Comparing the stretching technique and the wavelet cross-spectrum technique for measuring stress-induced wave-velocity changes in concrete

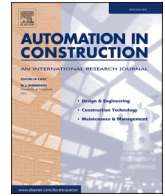Cheng, Hao; Weemstra, Cornelis; Hendriks, Max A.N.; Yang, Yuguang

Important note
To cite this publication, please use the final published version (if applicable).
Please check the document version above.

Comparing the stretching technique and the wavelet cross-spectrum technique for measuring stress-induced wave-velocity changes in concrete

Hao Cheng [a,*], Cornelis Weemstra [b], Max A.N. Hendriks [a,c], Yuguang Yang [a]

[a] *Department of Engineering Structures, Faculty of Civil Engineering and Geosciences, Delft University of Technology, Stevinweg 1, 2628 CN Delft, the Netherlands*
[b] *Department of Geoscience and Engineering, Faculty of Civil Engineering and Geosciences, Delft University of Technology, Stevinweg 1, 2628 CN Delft, the Netherlands*
[c] *Department of Structural Engineering, Faculty of Engineering, Norwegian University of Science and Technology, 7491 Trondheim, Norway*

ARTICLE INFO

ABSTRACT

Coda wave interferometry (CWI) holds promise as a technique for concrete stress monitoring. This is because the coda, which consists of multiply scattered arrivals, is the result of propagation through the medium over large distances. As such, it is sensitive to both minute structural changes and small velocity changes in that medium. Previous studies focusing on concrete have predominantly utilized the time-domain-based stretching technique to measure travel-time changes. There is, however, a lack of consensus on how to quantify these changes effectively. In this study, we conduct a systematic comparison between two techniques, namely the stretching technique and the wavelet cross-spectrum (WCS) technique, for measuring stress-induced velocity changes in a cylindrical concrete sample. Our comparison focuses on two key aspects: (i) stability against cycle skipping and (ii) consistency in retrieving velocity changes. Experimental results reveal that both the WCS technique and the stretching technique yield consistent velocity changes. In terms of stability, it is challenging to determine which technique performs better, due to differences in the mechanisms triggering cycle skipping. However, when considering waves with frequencies ranging from 50 kHz to 80 kHz, both techniques exhibit comparable performance. Based on our findings, we offer the following recommendations for utilizing these CWI techniques in concrete stress monitoring:

For the stretching technique, selecting the time window length based on the wave frequency and the expected magnitude of velocity change.

For the WCS technique, operating it in the frequency band where spectral decomposition shows sufficiently high energy in the signal and can accommodate the expected magnitude of velocity change.

1. Introduction

Due to the prevalence of concrete in civil structures, monitoring and evaluating the structural health (often referred to as structural health monitoring or its acronym SHM) of concrete structures are receiving increased attention [1–4]. In this context, monitoring stress variations in concrete structures (both in time and space) is of vital importance. Among the existing methods for monitoring stress in concrete [5–8], elastic wave-based coda wave interferometry (CWI) is arguably the most promising. In particular, because of the coda's high sensitivity to weak changes in the medium and its relatively large reach [9–12].

CWI exploits the coda of elastic waves; the underlying theory is described, to a considerable extent, in the articles [13,14]. The term *coda*, first proposed by Aki [15], refers to the tail of the seismograms and

hence is synonymous with the 'later-arriving multiply scattered waves' [16]. The complex superposition of these scattered waves leads to an irregular waveform, which might appear as noise. However, coda waves are reproducible [9]. The high sensitivity of CWI can be explained by the long propagation path, which allows the effect of weak perturbations in the medium to be accumulated. In the context of structural health monitoring of concrete, such weak perturbations are usually the result of (i) the development of micro-cracks or (ii) stress changes. The former can be quantified using waveform changes [10,12,17], whereas the latter manifest themselves merely as travel time (or arrival-time) changes due to the acoustoelastic effect [18,19]. Here, it should be understood that this is a two-step process: the acoustoelastic effect leads to velocity changes in the medium, which in turn lead to travel time changes of elastic waves. In this article, the retrieval of stress-induced

velocity changes in concrete will be the main subject of investigation.

Although CWI is a relatively new approach in the field of SHM, various attempts to retrieve stress-induced velocity changes in concrete have been reported. These attempts are summarized in Table 1, which shows that only time-domain-based techniques are adopted in the current (SHM) literature and that there is no consensus on the ideal time window length. By exclusively relying on time-domain-based techniques, the potential frequency dependence of the retrieved travel time changes is ignored and hence cannot be evaluated. And because the frequency is not a parameter in bulk wave acoustoelasticity [18–20], some researchers assume that the retrieved travel time change is a constant among different frequency components [21]. This has not been validated. In order to do so, it is crucial to utilize a frequency-domain-based technique to examine the stress-induced velocity changes. In this study, we therefore draw from recent developments in the field of seismology to introduce and test frequency-domain-based CWI techniques for the purpose of stress monitoring in concrete.

In seismology, five CWI techniques currently dominate the estimation of travel time changes: the Moving Window Cross-Correlation (MWCC) [14,43], the Moving Window Cross-Spectrum (MWCS) [44,45], the stretching technique [46], the Dynamic Time Warping (DTW) [47] and the Wavelet Cross-Spectrum (WCS) technique [48]. A performance comparison of these five techniques is reported by Yuan et al. [49] using numerical simulations (i.e., the correct value is known). They use five criteria to evaluate their performance: (operated) domain, availability of the Correlation Coefficient (CC), frequency resolution, stability, and accuracy. Their conclusions are summarized in Table 2.

The *operated domain* describes which domain the CWI technique operates in. Studies involving the application of CWI for measuring stress-induced velocity changes in concrete only use time-domain-based techniques (see Table 1). The determination of travel time changes in the transform domain may improve the computation speed and filter the environmental noise (this will be further discussed in the discussion section). The *availability of the CC (*second criterion) indicates whether the 'correlation coefficient' between the perturbed and unperturbed signal becomes available using that technique. Although the correlation coefficient, or alternatively the 'decorrelation', is chiefly used for crack localization [10,12,30], this parameter also quantifies the reliability of the retrieved travel time change [32]. That is, the travel time change is meaningful only when the perturbed and unperturbed signals are sufficiently similar [48], which is reflected by the magnitude of the correlation coefficient. The *time-frequency resolution* points to the minimum resolution in both time and frequency that can be resolved. Since time-domain-based techniques operate in the time domain, the frequency resolution of these techniques is poor. For transform-domain-based techniques, WCS has better time-frequency resolution than MWCS [48]. The fourth criterion, *stability,* evaluates whether the estimated travel time change is temporally stable. When it comes to this aspect, the performance of the different techniques involves their ability to mitigate 'cycle skipping', a phenomenon that one wiggle in the signal associated with the perturbed medium aligns with a wiggle in the signal associated with the unperturbed state that is displaced by approximately one period [47]. Finally, the *accuracy* is the degree to which the estimated travel time change corresponds to the correct value. In the article [49], the authors conclude that DTW and the stretching technique have greater accuracy compared to other techniques. They also mention that the modest performance of MWCS and the WCS technique is attributed to low energy at specific frequencies. If one operates the WCS technique in a frequency range with sufficient energy, it has a better performance than MWCS according to Mao et al. [48]. It should be noted that the assessment of the accuracy of the WCS technique in Yuan et al. [49] involves the application of this technique to a broad frequency band.

The objective of this paper is to compare the performance of time-domain- and transform-domain-based techniques when it comes to the estimation of (stress-induced) velocity changes in concrete. Given that the performance of time-domain-based techniques has already been demonstrated for measuring stress-induced velocity changes in concrete, while this is not the case for transform-domain-based techniques, their

Table 1
Recent studies on retrieving the stress-induced velocity changes in concrete using CWI.

Literature	Specimen dimensions [mm]	CWI technique	Time window length [μs]
Larose et al. 2009 [22]	Cylinder Ø160 × 285	Stretching	450
Payan et al. 2009 [23]	Cylinder Ø75 × 160	MWCC*	20
Payan et al. 2010 [24]	Cylinder Ø75 × 160	MWCC	NM**
Lillamand et al. 2010 [25]	Cylinder Ø70 × 135	MWCC	NM
Payan et al. 2011 [26]	Cylinder Ø75 × 160	MWCC	20
Schurr et al. 2011 [27]	Prism 305 × 76 × 76	Stretching	NM
Stähler et al. 2011 [21]	Cube 150 × 150 × 150	Stretching	NM
Zhang et al. 2012 [28]	Cylinder 110 × 450	Stretching	200
Zhang et al. 2013 [29]	Cylinder 110 × 450	Stretching	200
Zhang et al. 2016 [30]	Beam 6100 × 1600 × 800	Stretching	500
Zhang et al. 2018 [31]	Cube 100 × 100 × 100	Stretching	50/75
Clauß et al. 2020 [32]	Beam 2000 × 150 × 400	Stretching	NM
Jiang et al. 2020 [33]	Beam 5960 × 870 × 300	Stretching	NM
Zhan et al. 2020 [34]	T-beam 29,200 × 1700 × 1600	Stretching	NM
Zhan et al. 2020 [35]	Prism 300 × 150 × 150	Stretching	40
Hu et al. 2021 [36]	Cube 150 × 150 × 150	Stretching	257
Jiang et al. 2021 [37]	Beam 5960 × 870 × 300 T-beam 29,200 × 1700 × 1600	Stretching	2000/6000
Xue et al. 2021 [38]	Concrete Containment	Stretching	320
Zhong et al. 2021 [39]	Cylinder Ø152 × 304 Prism 508 × 152 × 152	Stretching	14/150
Diewald et al. 2022 [40]	Prism 400 × 100 × 100 Bone-shaped cylinder	Stretching	NM
He et al. 2022 [41]	Cube 150 × 150 × 150 100 × 100 × 100	Stretching	NM
Zhong et al. 2022 [42]	Cylinder Ø100 × 200	Stretching	200

Note: * MWCC: Moving Window Cross-Correlation.
** NM: Not Mentioned.

Table 2
Criteria used by Yuan et al. [49] to compare five techniques for retrieving coda wave travel time changes.

CWI technique	MWCC	MWCS	Stretching	DTW	WCS
Operated domain	Time	Fourier	Time	Time	Wavelet
Availability of *CC*	Yes	Yes	Yes	No	Yes
Time-frequency resolution	Low	Medium	Low	Low	High
Stability	Low	Low	Medium	High	Unknown
Accuracy	Low	Low*	High	High	Medium*

Note: * only valid when the signal energy at frequencies of interest is high.

consistency (or lack of consistency) in determining travel time changes needs to be assessed. Furthermore, the stability of time-domain- and transform-domain-based CWI techniques in retrieving velocity changes in concrete will also be examined. The theory underlying the selected time-domain- and transform-domain-based techniques are introduced in Section 2. Additionally, a brief introduction to acoustoelasticity is given in this section. The conclusions listed in Table 2 are drawn based on the techniques' application in the field of seismology. The application of CWI to concrete structures involves, however, rather different frequencies of interest and magnitudes of velocity changes. In this study, we therefore perform a quantitative comparison of the stretching technique and the WCS technique for the purpose of CWI applied to concrete structures. To this end, a dedicated experimental study that is representative for typical applications of CWI to concrete structures is executed. The details of this experiment can be found in Section 3, and its results are presented in Section 4. In Section 5, a discussion is presented on the cycle skipping, computational efficiency, future applications, and some recommendations for future work. Finally, the conclusion is provided in Section 6.

2. Theory

In this section, the theoretical foundations of the selected CWI techniques are given, and the acoustoelastic effect is introduced. The stretching technique is chosen as the time domain technique because it combines high accuracy with reasonable stability. The theoretical background of this technique can be found in Section 2.1. The WCS technique, which has higher accuracy and better time-frequency resolution than MWCS, is selected as the transform-domain-based technique. The theoretical background of the WCS technique is shown in Section 2.2. Theoretical velocity-stress relationships, also known as the acoustoelastic effect, are introduced in Section 2.3.

2.1. The stretching technique

$$U_{\mathrm{unp}}^{(t_c)}(f) \equiv F\left\{ u_{\mathrm{unp}}^{(t_c)}(t) \right\}$$
$$= A_{\mathrm{unp}}(f)e^{j\varphi_{\mathrm{unp}}(f)}, \tag{2a}$$

$$U_{\mathrm{per}}^{(t_c)}(f,\varepsilon) \equiv F\left\{ u_{\mathrm{per}}^{(t_c)}(t(1-\varepsilon)) \right\}$$
$$= \frac{1}{1-\varepsilon}U_{\mathrm{per}}^{(t_c)}\left(\frac{f}{1-\varepsilon}\right)$$
$$\approx (1+\varepsilon)U_{\mathrm{per}}^{(t_c)}(f(1+\varepsilon)) \tag{2b}$$
$$= (1+\varepsilon)A_{\mathrm{per}}(f(1+\varepsilon))e^{j\varphi_{\mathrm{per}}(f(1+\varepsilon))},$$

where f is the frequency, $A_{\mathrm{unp}}(f)$ and $A_{\mathrm{per}}(f)$ are amplitude spectra, and $\varphi_{\mathrm{unp}}(f)$ and $\varphi_{\mathrm{per}}(f)$ are phase spectra. Eq. (2) shows that stretching a signal affects both amplitude and phase. Therefore, Eq. (1) can be rewritten as [51].

$$CC(t_c, T, \varepsilon) = \frac{\int_{-\infty}^{+\infty} U_{\mathrm{per}}^{(t_c)}(f,\varepsilon)\left[U_{\mathrm{unp}}^{(t_c)}(f)\right]^* df}{\sqrt{\int_{-\infty}^{+\infty} U_{\mathrm{unp}}^{(t_c)}(f)\left[U_{\mathrm{unp}}^{(t_c)}(f)\right]^* df}\sqrt{\int_{-\infty}^{+\infty} U_{\mathrm{per}}^{(t_c)}(f,\varepsilon)\left[U_{\mathrm{per}}^{(t_c)}(f)\right]^* df}}$$
$$= \frac{\int_{-\infty}^{+\infty} A_{\mathrm{unp}}(f)A_{\mathrm{per}}(f(1+\varepsilon))e^{j\left[\varphi_{per}(f(1+\varepsilon))-\varphi_{\mathrm{unp}}(f)\right]} df}{\sqrt{\int_{-\infty}^{+\infty} A_{\mathrm{unp}}^2(f)df}\sqrt{\int_{-\infty}^{+\infty} A_{\mathrm{per}}^2(f(1+\varepsilon))df}}, \tag{3}$$

where the asterisk denotes complex conjugation. Both the relation between the numerator in Eq. (1) and (3), and the denominator in Eq. (1) and (3) follow from Parseval's theory (see Appendix A). Note that although the expression at the right-hand side of Eq. (3) contains imaginary terms, its absolute value coincides with the *CC* obtained through the application of Eq. (1). Explicitly, this is written as [52]:

$$|CC(t_c, T, \varepsilon)| = \sqrt{\frac{\int_{-\infty}^{+\infty} A_{\mathrm{unp}}(f)A_{\mathrm{per}}(f(1+\varepsilon))e^{j\left[\varphi_{\mathrm{per}}(f(1+\varepsilon))-\varphi_{\mathrm{unp}}(f)\right]} df \int_{-\infty}^{+\infty} A_{\mathrm{unp}}(f)A_{\mathrm{per}}(f(1+\varepsilon))e^{-j\left[\varphi_{\mathrm{per}}(f(1+\varepsilon))-\varphi_{\mathrm{unp}}(f)\right]} df}{\int_{-\infty}^{+\infty} A_{\mathrm{unp}}^2(f)df \int_{-\infty}^{+\infty} A_{\mathrm{per}}^2(f(1+\varepsilon))df}}. \tag{4}$$

The stretching technique [50] is an improvement of MWCC. It assumes a linear increase or decrease of the lag time. Implicitly, the velocity disturbance in the medium is assumed to be homogeneous [46]. This technique calculates the correlation coefficients of windowed signals recorded in an unperturbed state, u_{unp}, and signals recorded after (or during) the perturbation, u_{per}, in the time domain using

$$CC(t_c, T, \varepsilon) = \frac{\int_{t_c-T}^{t_c+T} u_{\mathrm{unp}}^{(t_c)}(t)u_{\mathrm{per}}^{(t_c)}(t(1-\varepsilon))\mathrm{d}t}{\sqrt{\int_{t_c-T}^{t_c+T}\left[u_{\mathrm{unp}}^{(t_c)}(t)\right]^2\mathrm{d}t}\sqrt{\int_{t_c-T}^{t_c+T}\left[u_{\mathrm{per}}^{(t_c)}(t(1-\varepsilon))\right]^2\mathrm{d}t}}, \tag{1}$$

where the time window is centred at time t_c with a duration of 2 T and ε denotes the stretching factor, representing the relative change in travel time dt/t. In case of a uniform velocity change dv in the medium, the stretching factor that maximizes $CC(t_c,T,\varepsilon)$, $\varepsilon_{\mathrm{max}}$, coincides with the velocity change in the medium, dv/v. Although the stretching technique is operated in the time domain, it can also be represented in the frequency domain. Letting the Fourier transforms of $u_{\mathrm{unp}}^{(t_c)}(t)$ and $u_{\mathrm{per}}^{(t_c)}(t(1-\varepsilon))$ be $U_{\mathrm{unp}}^{(t_c)}(f)$ and $U_{\mathrm{per}}^{(t_c)}(f,\varepsilon)$, and assuming that ε is much smaller than 1, then

This quantity is usually referred to as the 'coherency' and expresses the stretching technique in the frequency domain.

Compared with MWCC, the stretching technique is more stable in the presence of noise [53]. Furthermore, this technique can deal with a larger time window without compromising accuracy and is more robust when it comes to cycle skipping [47].

2.2. The WCS technique

The WCS technique is a relatively new CWI technique proposed by Mao et al. [48]. This technique relies on the phase of the wavelet cross-spectrum, which is related to the time shift between two signals.

In application, the signal is first transformed to the wavelet domain using the continuous wavelet transform (CWT). In this paper, the analytical Morlet wavelet [54,55] is chosen as the mother wavelet since it has equal variance in time and frequency. We designed the analytical Morlet-based CWT filter bank in the frequency domain, where the filter bank $\Phi(f_l^{(c)}, f_n)$ is defined as

$$\Phi\left(f_i^{(c)}, f_n\right) = 2 \times H(f_n) \times e^{-\frac{\left[s\left(f_i^{(c)}\right)f_n - \omega_0\right]^2}{2}}, n \in [1, N], \quad (5a)$$

$$S\left(f_i^{(c)}\right) = \omega_0 \frac{f_{\text{Nyquist}}}{f_i^{(c)}}, i \in [1, M], \quad (5b)$$

where f_n, f_{Nyquist} and $f_i^{(c)}$ represent the frequency components of the filter, the Nyquist frequency, and the centre frequency of the filter, respectively. The parameter N represents the total number of sampling points of the signal in the time domain. The amount of filters in the filter bank is M. The functions $H(\cdot)$ and $S(f_i^{(c)})$ are the Heaviside step function and scale function, respectively. The constant ω_0 is set to 6 to satisfy the admissibility condition, which requires the mother wavelet to be zero-mean [56]. For more details about the admissibility condition, we recommend readers the article from Farge [56]. The designed CWT filter bank is multiplied with the target signal in the frequency domain, and then transformed back to time domain through the inverse fast Fourier transform (IFFT). The obtained time-frequency spectrum is dubbed the wavelet spectrum $W(f_i^{(c)}, t_n)$, where t_n is the sampling point in the time domain.

After operating the CWT, the wavelet cross-coherency $\Gamma(f_i^{(c)}, t_n)$ can be calculated through the obtained wavelet spectra of the signal before perturbation, $W_{\text{unp}}(f_i^{(c)}, t_n)$, and after perturbation, $W_{\text{per}}(f_i^{(c)}, t_n)$,

$$\rho_0 v_{11}^2 = \lambda + 2\mu + \frac{\sigma_{11}}{3K}\left[2l + \lambda + \frac{\lambda + \mu}{\mu}(4m + 4\lambda + 10\mu)\right], \quad (7a)$$

$$\rho_0 v_{22}^2 = \rho_0 v_{33}^2 = \lambda + 2\mu + \frac{\sigma_{11}}{3K}\left[2l - \frac{2\lambda}{\mu}(m + \lambda + 2\mu)\right], \quad (7b)$$

$$\rho_0 v_{12}^2 = \rho_0 v_{13}^2 = \mu + \frac{\sigma_{11}}{3K}\left[m + 4\lambda + 4\mu + \frac{\lambda n}{4\mu}\right], \quad (7c)$$

$$\rho_0 v_{21}^2 = \rho_0 v_{31}^2 = \mu + \frac{\sigma_{11}}{3K}\left[m + \lambda + 2\mu + \frac{\lambda n}{4\mu}\right], \quad (7d)$$

$$\rho_0 v_{23}^2 = \rho_0 v_{32}^2 = \mu + \frac{\sigma_{11}}{3K}\left[m - 2\lambda - \frac{\lambda + \mu}{2\mu}n\right], \quad (7e)$$

where v is the wave velocity. The first subscript of v is related to the wave propagation direction, and the second subscript represents its polarization direction. The parameters l, m and n are Murnaghan constants, and λ and μ are Lamé parameters. The parameters K and ρ_0 represent bulk modulus and density, respectively. By introducing the acoustoelastic tensor A_{ijpq}, equations in Eq. (7) can be written as

$$v_{ij} = v_{ij}^0 \sqrt{1 + 2A_{ijpq}\sigma_{pq}}, \quad i, j, p, q \in \{1, 2, 3\}, \quad (8)$$

$$\Gamma\left(f_i^{(c)}, t_n\right) = \frac{\varsigma\left\{\left[s\left(f_i^{(c)}i\right)\right]^{-1}W_{\text{unp,per}}\left(f_i^{(c)}i, t_n\right)\right\}}{\sqrt{\varsigma\left\{\left[s\left(f_i^{(c)}\right)\right]^{-1}W_{\text{unp,unp}}\left(f_i^{(c)}, t_n\right)\right\}\varsigma\left\{\left[s\left(f_i^{(c)}\right)\right]^{-1}W_{\text{per,per}}\left(f_i^{(c)}, t_n\right)\right\}}}$$

$$= \frac{\varsigma\left\{\left[s\left(f_i^{(c)}i\right)\right]^{-1}W_{\text{unp}}\left(f_i^{(c)}i, t_n\right)W_{\text{per}}^*\left(f_i^{(c)}i, t_n\right)\right\}}{\sqrt{\varsigma\left\{\left[s\left(f_i^{(c)}i\right)\right]^{-1}\left|W_{\text{unp}}\left(f_i^{(c)}i, t_n\right)\right|^2\right\}\varsigma\left\{\left[s\left(f_i^{(c)}\right)\right]^{-1}\left|W_{\text{per}}\left(f_i^{(c)}i, t_n\right)\right|^2\right\}}}, \quad (6)$$

where $s(f_i^{(c)})$ represents the wavelet scale [57] and can be calculated through dividing $S(f_i^{(c)})$ in Eq. (5b) by the sampling rate. The symbol $\varsigma\{\cdot\}$ denotes the smoothing operator for both time and frequency scales to prevent the coherency being identically one [58]. The phase angle of the wavelet cross-coherency $\Gamma(f_i^{(c)}, t_n)$ is the phase difference spectrum $\phi_{\text{unp,per}}(f_i^{(c)}, t_n)$. This phase difference spectrum can be converted into the time difference spectrum $\delta t_{\text{unp,per}}(f_i^{(c)}, t_n)$ through dividing by $2\pi f_i^{(c)}$ at each frequency component. The velocity change spectrum $dv/v_{\text{unp,per}}(f_i^{(c)}, t_n)$ can be obtained using the $\delta t_{\text{unp,per}}(f_i^{(c)}, t_n)$ divided by the lapse time t at each lapse time.

Compared with the Fourier transform-based MWCS, in which the time window length is fixed, the time window length of the wavelet adapts to each frequency (continuous wavelet transform) and hence has a better time-frequency resolution [48]. Another advantage of WCS technique is its higher computational speed, especially compared to time-domain-based techniques [48]. The drawbacks of WCS technique is poor performance in estimating the velocity change at frequencies with low energy [48,49], which will be further discussed in the discussion section.

2.3. The acoustoelastic effect

The acoustoelastic effect describes how the wave velocities change in a stressed medium [59]. The body wave acoustoelasticity in the medium with uniaxial stress σ_{11} applied in 1-direction can be represented by using following equations [18].

where v_{ij} and v_{ij}^0 represent the wave velocity under axial stress and without axial stress applied; i and j represent wave propagation and polarization directions, respectively; p and q are related to the uniaxial stress direction ($p = q$). After linearization, this equation can be simplified to [25].

$$v_{ij} \approx v_{ij}^0\left(1 + A_{ijpq}\sigma_{pq}\right), \quad (9)$$

where i and j represent the wave propagation and polarization directions, respectively. Since the stress (at rest) is usually a certain stress level σ_0 rather than 0 MPa in most cases, Eq. (9) should be rewritten as

$$\frac{v_{ij}^\sigma - v_{ij}^{\sigma_0}}{v_{ij}^{\sigma_0}} = \frac{A_{ijpq}}{1 + A_{ijpq}\sigma_{pq}^0}\left(\sigma_{pq} - \sigma_{pq}^0\right). \quad (10)$$

Considering that the magnitude of $A_{ijpq}\sigma_{pq}^0$ is much smaller than 1 in concrete [60], Eq. (10) can be further simplified into

$$\frac{v_{ij}^\sigma - v_{ij}^{\sigma_0}}{v_{ij}^{\sigma_0}} \approx A_{ijpq}\left(\sigma_{pq} - \sigma_{pq}^0\right). \quad (11)$$

As shown in Eq. (11), the slope of the velocity change is approximately equal to the acoustoelastic parameter.

3. Experimental design

The selected CWI techniques are further verified in a dedicated experiment in our lab. Considering that the wavelength of an S-wave
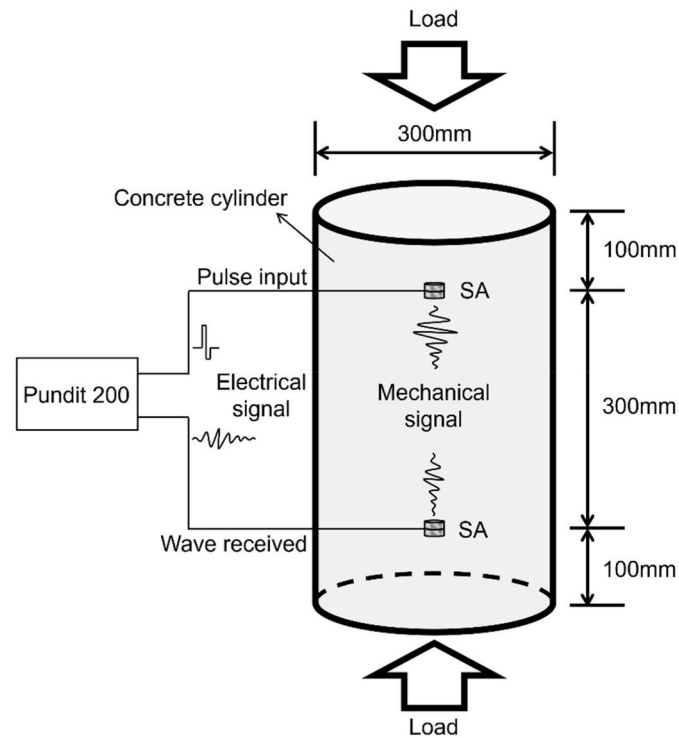
(a) Concrete cylindrical sample with SA locations and data acquisition device (note that there is some vertical exaggeration).

(b) Photo of an SA.

Fig. 1. Concrete sample and Smart Aggregate (SA).

associated with the lowest frequency of interest (50 kHz) coincides with approximately 54 mm (assuming an S-wave speed of approximately 2700 m/s, which is typical for concrete), a cylindrical sample with a diameter of 300 mm and a height of 500 mm is designed. We use a typical commercial concrete mixture with a compressive strength grade of C50/60. The load is applied axially by means of a gypsum layer and a wooden plate on top of the top surface of the cylinder. The diagram of the concrete sample is shown in Fig. 1(a).

Because Rayleigh waves only propagate along the surface of the sample (we focus on body waves), two piezoelectric sensors with the polarization direction parallel to the load direction are embedded inside this cylinder. Such embeddable sensors may act as both source and receiver, and are usually referred to as smart aggregates (SA) [61]. The photo of an SA is shown in Fig. 1(b). An SA is, potentially, an ideal sensor for long-term infrastructure monitoring due to its high durability and low cost [11,62,63]. SAs also facilitate the application of CWI in civil engineering, since CWI requires less environmental variation and strong coupling during its usage. The minimum distance from the SA to the

surface of the specimen is 100 mm (top/bottom surface). Considering that the frequencies of interest exceed 50 kHz, and that the Rayleigh wave velocity in concrete is around 2300 m/s [64], the maximum effective depth of penetration of Rayleigh wave is about 46 mm [65]. This is obviously smaller than 100 mm, implying that the presence of Rayleigh wave-related particle velocities in our measurements can be neglected. Sensor locations are also depicted in Fig. 1(a).

The typical target compressive stress range for a prestressed concrete bridge with a concrete grade of C50/60 during its service life is 7 MPa to 12 MPa, which can be considered to be representative to the expected application scenario. The loading and unloading processes are repeated 3 times. The loading protocol is designed based on this stress range and shown in Fig. 2. The first and second cycles are loaded from 500 kN (7.07 MPa) to 700 kN (9.90 MPa) and back to 500 kN (7.07 MPa) with a 10 kN (0.14 MPa) interval. The third cycle starts from 500 kN (7.07 MPa) but go higher to 800 kN (11.32 MPa) and back to 400 kN (5.66 MPa) with the same interval. The loading and unloading processes are coloured in red and green in Fig. 2, respectively. There are 151 loading
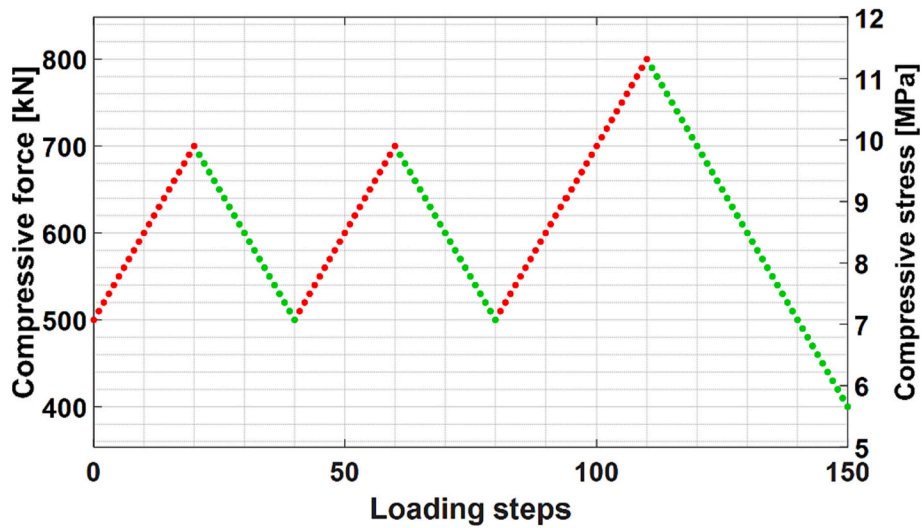
Fig. 2. Loading protocol (red dots are associated with loading stages, green dots with unloading). (For interpretation of the references to colour in this figure legend, the reader is referred to the web version of this article.)

steps in total, as shown on the *x*-axis, and the first loading step is counted as load step 0. The loading speed during both the loading and unloading processes is maintained at 0.5 kN/s, which translates to 7.07 kPa/s. Upon reaching each load step, there is an initial one-minute waiting period to ensure stability in the loading jack before measurements are taken. The measurement at each loading step is completed in less than one minute.

A portable ultrasonic system, Pundit 200, is used at each load step to
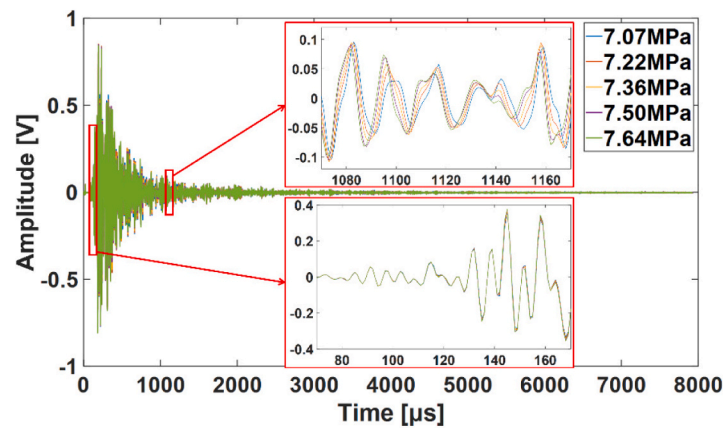
(a) Signals at Loading Step 0 (7.07 MPa), 1 (7.22 MPa), 2 (7.36 MPa), 3 (7.50 MPa), and 4 (7.64 MPa).
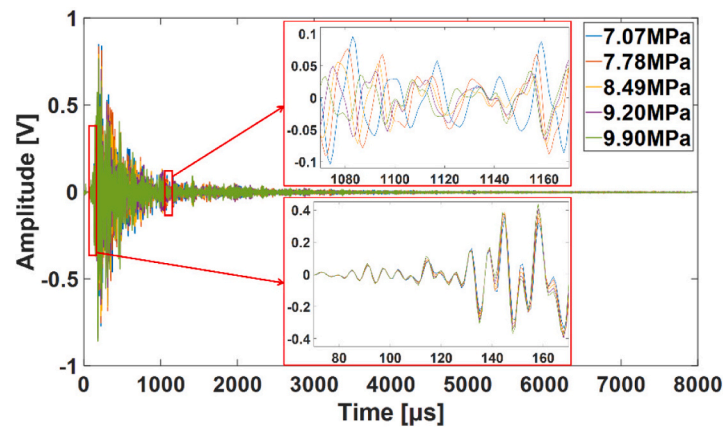
(b) Signals at Loading Step 0 (7.07 MPa), 5 (7.78 MPa), 10 (8.49 MPa), 15 (9.20 MPa), and 20 (9.90 MPa).

Fig. 3. Received signals in the time domain. The time window from 70 μs to 170 μs contains the direct wave and the first scattered arrivals, whereas the time window from 1070 μs to 1170 μs contains multiply scattered waves.

generate and receive the ultrasonic signal. Considering the resonant frequency of SA, around 80 kHz [66], and frequency of interest, higher than 50 kHz, a squared pulse with a frequency of 54 kHz is used as the excitation signal. The SA utilized in this paper operates in compressive mode, with the PZT patch functioning in d_{33} mode. This specific SA primarily generates P-waves once it begins vibrating within the concrete. The sampling rate is 1 MHz. Since the test was carried out in the lab with a small temperature fluctuation, we propose that velocity variations are mainly caused by stress change. The wave analysis techniques, including the wavelet transform, the stretching technique and the WCS technique, are executed within the MATLAB environment.

4. Comparison of the WCS technique and the stretching technique

The comparison between WCS technique and stretching technique is detailed in this section. In Section 4.1, we first perform a time-frequency analysis of the signals. The parameters for the CWI techniques are selected based on the time-frequency characteristics and shown in Section 4.2. The comparison in terms of stability, retrieved velocity change, retrieved acoustoelastic effect, and consistency in estimation velocity change are discussed separately in Sections 4.3, 4.4, 4.5, and 4.6, respectively.

4.1. Time-frequency analysis

The signals measured at the first five loading steps (Step 0–4) are shown in Fig. 3(a). The stress linearly increases with steps of 0.14 MPa. With such small stress changes, the direct waves are almost identical, and the time shift is not visible. However, the time shift is evident in the coda, whereas the waveforms still have almost the same form. Upon reaching a higher stress level of approximately 9.90 MPa, as illustrated in Fig. 3(b), the waveform of the direct waves remains indistinguishable, but the time shifts become more pronounced compared to Fig. 3(a). In the coda, the time shifts become substantial, and the similarity between waveforms decreases, particularly between the signals recorded at 7.07 MPa and 9.90 MPa. This reduced waveform similarity indicates that there have been changes in the wave paths, likely due to the development of microcracks at the interface between coarse aggregates and cement matrix during loading, along with a reduction in the volume of air voids and pores during concrete compression. The result shown in Fig. 3(b) also suggests that directly applying CWI to the signals recorded
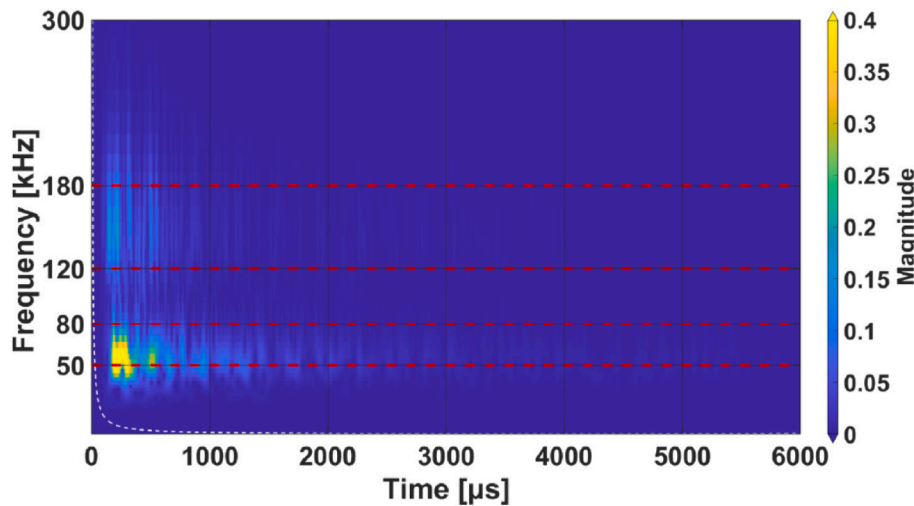
(a) 5.66 MPa (load step 150).
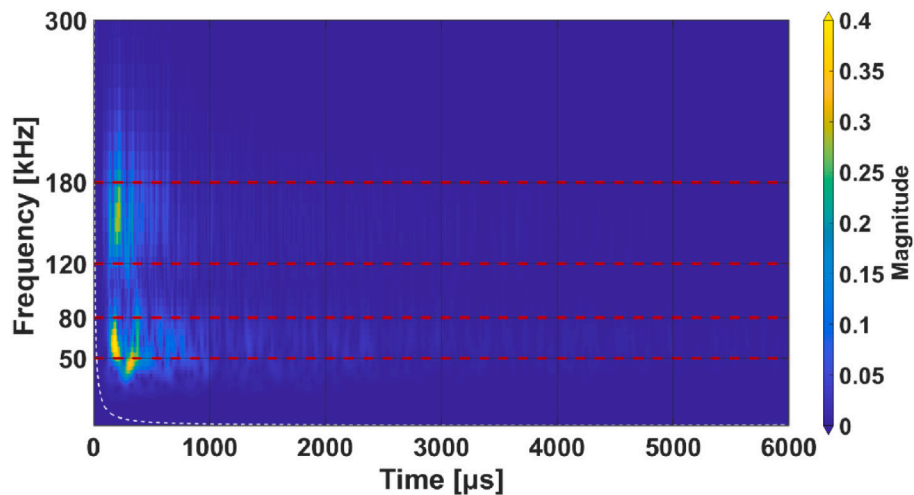
(b) 11.32 MPa (load step 110).

Fig. 4. Time-frequency spectra of signals at load step 150 and load step 110. The energy concentrates in two frequency bands, 50–80 kHz and 120–180 kHz, highlighted using red dashed lines. (For interpretation of the references to colour in this figure legend, the reader is referred to the web version of this article.)

at 7.07 MPa and 9.90 MPa may not be ideal in applications, given the relatively low waveform similarity between these two cases in the coda.

In this paper, the time-frequency analysis is realized using the CWT (i.e., a filter bank). The centre frequencies of the filter bank require the input of the frequency range and the number of voices per octave, a parameter related to the sampling density of the frequency scale. The frequency range is selected from 50 Hz to Nyquist frequency, 500 kHz, and the number of voices per octave is 10.

Fig. 4 shows the time-frequency spectra of the signals at Step 150 (5.66 MPa) and Step 110 (11.32 MPa), respectively. From the magnitude of the CWT, we find that the energy concentrates in two frequency bands: one roughly from 50 kHz to 80 kHz, and the other from 120 kHz to 180 kHz.

### 4.2. Parameters for CWI techniques

For the stretching technique, the time window length is an important parameter. In this paper, we adopted the criterion in Rossetto et al. [67] that the time window should contain at least five periods to prevent cycle skipping and mitigate strong fluctuations of the *CC*. To be on the safe side, the time window length for the stretching technique is therefore set to 200 μs, which is 10 times the reciprocal of 50 kHz and hence a time window contains at least ten periods. The time windows start just before the first arrival, and adjacent time windows overlap 100 μs (50%

overlap) to ensure the continuity of obtained ε_{max} or dv/v. In Section 4.3, the reference signal is fixed as the signal at load step 0. In Section 4.4, 4.5 and 4.6, relative dv/v are obtained by step-wise stretching [17], meaning that the signal at the previous loading step is always taken as the reference. The range of ε is from −1% to 1% with a step of 0.01‰. Considering the low signal-to-noise ratio (SNR) in the late coda, only the time windows before 6000 μs are used for the analysis. It is important to highlight that signals are not filtered when employing the stretching technique for velocity change retrieval.

As mentioned before, the WCS technique is only useful for obtaining the arrival-time changes at frequencies for which there is sufficient energy. Therefore, only the frequency bands between 50 and 80 kHz and between 120 and 180 kHz are adopted for the WCS analysis and referred to as the low-frequency regime (50–80 kHz) and the high-frequency regime (120–180 kHz). Just as for the stretching technique, the reference signal is set to be the signal at Step 0 in Section 4.3. In Section 4.4, 4.5 and 4.6, relative dv/v are obtained by step-wise WCS, where the reference signal is always associated with the previous loading step. The mother wavelet is again the analytic Morlet wavelet. To prevent the *CC* from being identically one [58], we adopted a similar smoothing approach as in Torrence and Webster [68]: a boxcar filter with a window length of three scales for scale smoothing and a Gaussian, $e^{-t^2/(2s^2)}$, for time smoothing. Considering the possible nonlinear relationship between time shift *dt* and lapse time *t* in the stressed concrete with complex
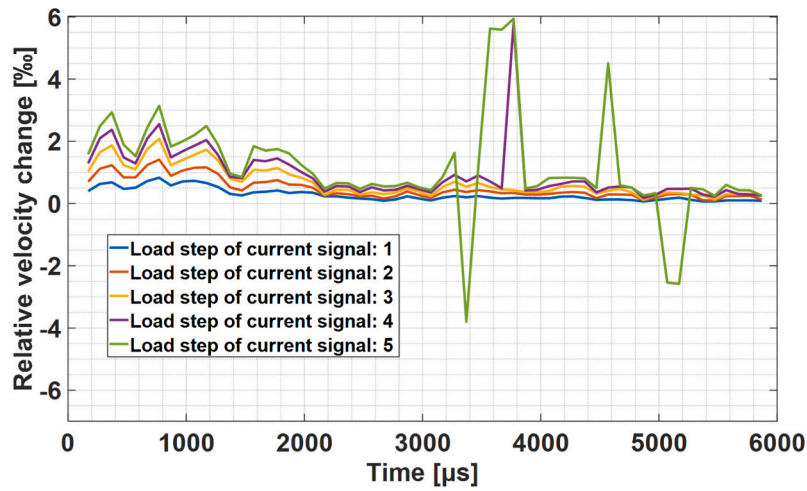
(a) Arrival-time difference as a function of lag time (i.e., t_c in Equation (1)).
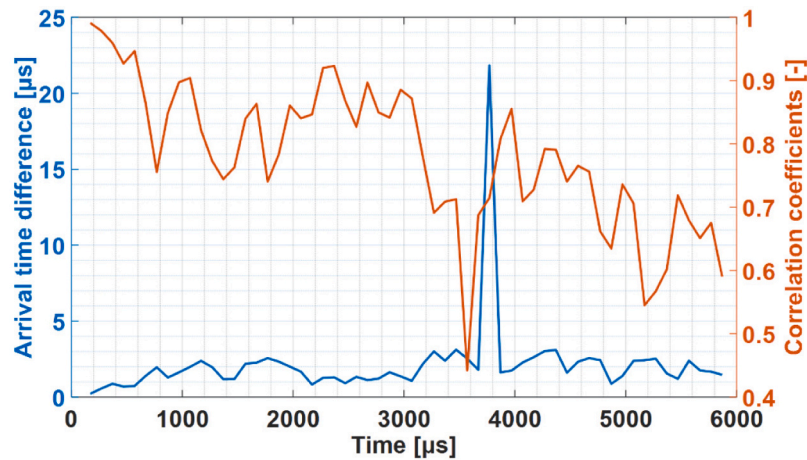
(b) Arrival time difference and *CC* as function of lag time (i.e., t_c in Equation (1)) with the current signal being the signal at loading step 4.

Fig. 5. Cycle skipping when using the stretching technique.

velocity perturbation, the linear regressions of dt versus t to obtain velocity change may not be applicable. However, the relationship between dt/t and dv/v is still valid. The time shift dt at each lapse time t is the mean travel time perturbation [13]; therefore, the velocity change dv/v obtained using the mean-time perturbation dt/t is the averaged velocity change [22].

4.3. Comparison between the stretching technique and the WCS technique: stability

As mentioned in Section 2, the stability of a CWI technique determines whether the obtained velocity changes are stable as a function of time. In case of low stability, anomalously large or small arrival-time differences can be observed, whereas the correlation coefficient remains fairly constant (and sufficiently high). A lack of stability is often due to the alignment of peaks which in reality are offset by approximately one period. This phenomenon is usually referred to as cycle skipping [47]. Effectively, the assessment of a CWI technique's stability therefore involves its ability to mitigate cycle skipping.

According to Mikesell et al. [47], the stretching technique is susceptible to cycle skipping when (i) the SNR is low, (ii) the time window is not long enough, or (iii) the reference and current signals diverge too

much. It has also been shown that cycle skipping is exacerbated when the bandwidth is narrow [47]. As the WCS technique yields a phase-based arrival-time difference, the origin of cycle skipping in this technique is different from that in the stretching technique. This will be discussed further below.

To ensure the occurrence of cycle skipping (for assessment purposes), the reference signal is set to be the signal at Step 0 for all computations in this subsection. The current signals are associated with loading steps 1 to 5. The inferred arrival-time difference relative to the signal at loading step 0 are shown in Fig. 5(a). It is important to emphasize that the stretching technique quantifies the relative arrival-time change (dt/t) between two traces. The arrival-time difference in Fig. 5 is obtained by multiplying this relative arrival-time change with the lag time (i.e., t_c in Eq. (1)). An anomalously high/low arrival-time difference is observed at around 3800 μs for the coda of the signal associated with loading step 4. Focussing on loading step 4, the arrival-time difference and *CC* are shown for all time windows in Fig. 5(b). It is found that cycle skipping occurs for time window 37, which has a central time t_c of 3780 μs, and despite the fact that the CC in this time window has a relatively high value of around 0.7.

As mentioned in Section 2.1, the stretching technique selects the stretching factor (ε) associated with the highest correlation coefficient.
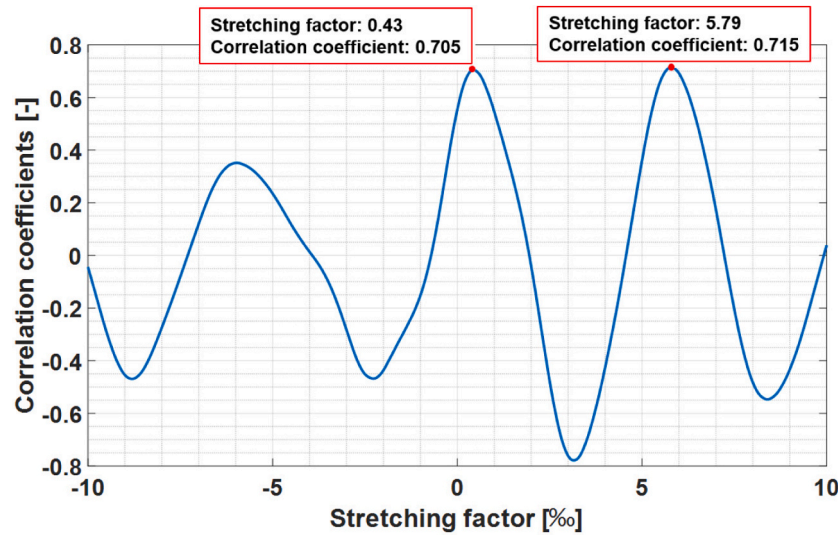
(a) Variation of the correlation coefficients with stretching factors.
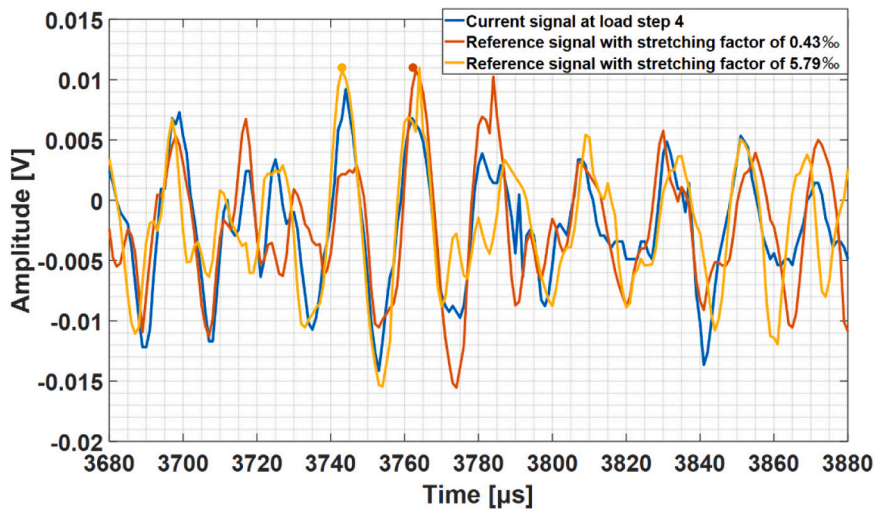

(b) Current signal and stretched signals with stretching factors highlighted in Figure 6(a).

Fig. 6. Stretching factors and stretched signals in the time window 37 (t_c = 3780 μs) when using the signal at Step 4 as the current signal.

Focussing on time window 37 ($t_c = 3780$ μs) of the signal recorded during loading step 4, we investigate how the correlation coefficient varies for different stretching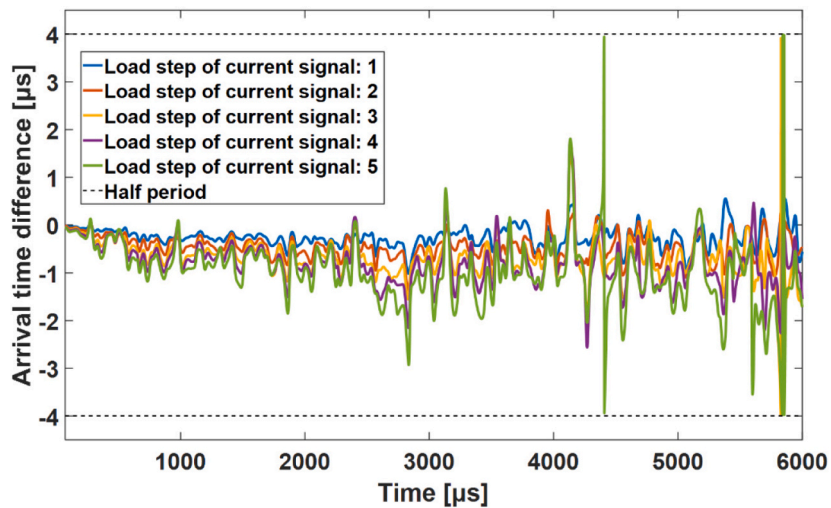 factors. Fig. 6(a) therefore displays the *CC* as a function of the employed stretching factor ε. Two almost equally high peaks can be observed, both with a relatively high correlation coefficient. The second peak is associated with a stretching factor of
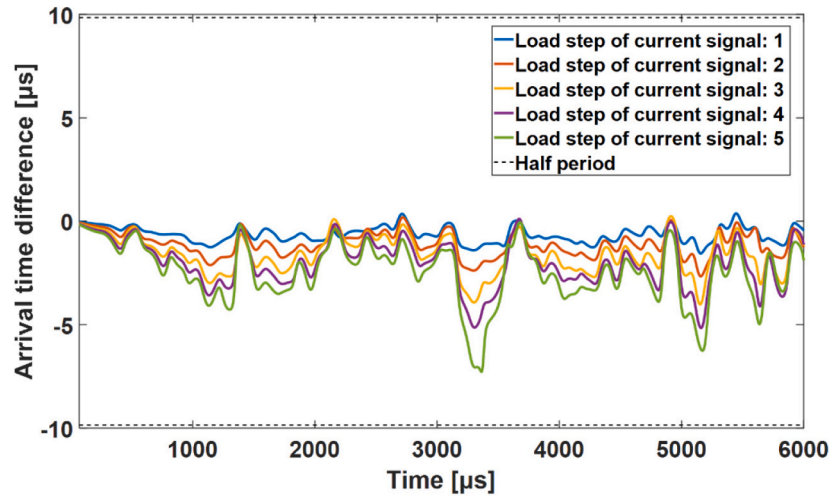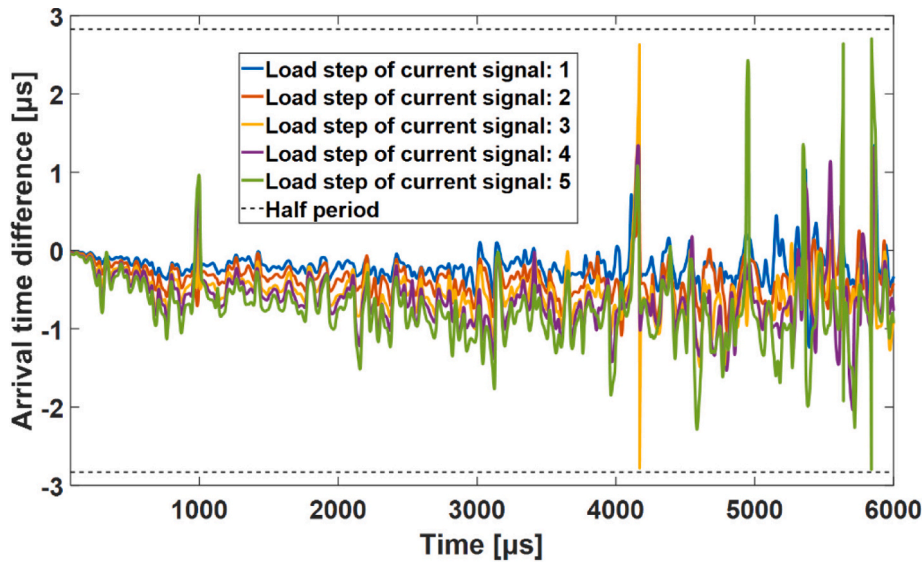

(a) 51 kHz.
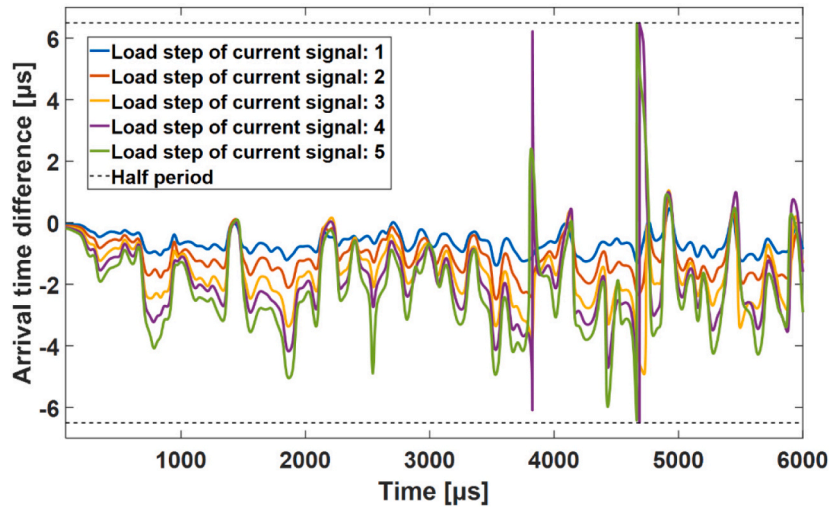
(b) 77 kHz.

(c) 125 kHz.

Fig. 7. Arrival-time difference of different frequency components as a function of lag time retrieved using the WCS technique.

(d) 177 kHz.

Fig. 7. (*continued*).

5.79‰. Since the *CC* attains its maximum for this value of *ε*, the stretching factor corresponding to this peak is selected. Plotting the stretched reference signals using the stretching factors associated with the two peaks, 0.43‰ and 5.79‰, together with the current signal, it can be observed that the time difference between the two stretched signals is indeed one cycle (the yellow and red dots shown in Fig. 6(b)). Here 'one cycle' corresponds to a time shift just below 20 μs, which corresponds to a frequency just over 50 kHz. Obviously, the true *ε* is not expected to be 5.79‰ since this value is significantly higher than the *ε* inferred for adjacent time windows (see Fig. 5(b)).

The main reason for the occurrence of cycle skipping is the decrease in SNR owing to the signal's amplitude attenuation. The strong noise masks the similarity between reference and current signals. Furthermore, because higher frequencies attenuate faster, the bandwidth becomes narrower with increasing lag time, further exacerbating cycle skipping [47]. In conclusion, the low SNR is the main trigger of cycle skipping while employing the stretching technique in this case. A similar result can be found in Mikesell et al. [47].

The cause of cycle skipping while employing the WCS technique differs from that of the stretching technique. The WCS technique is based on the phase spectrum in the wavelet domain, which implies that this technique can only measure phase changes from −π to +π. Consequently, the arrival-time differences corresponding with the phase difference spectrum range from a positive half period to a negative half period. Inferred arrival-time differences beyond this range will "jump" from one boundary to another, and corresponds to anomalously large arrival-time differences. Phase-based arrival-time differences are shown in Fig. 7 for four specific frequencies. The black dashed lines in Fig. 7 represent the arrival-time difference at positive and negative half periods for the considered frequency (equal to half the reciprocal of the frequency). As shown in Fig. 7(a), no arrival-time difference jumps from −π to +π (or vice versa) is observed, which suggests that cycle skipping does not occur at 51 kHz. This is due to the fact that the 51 kHz signal is able to accommodate a larger time shift and less affected by attenuation. However, for the higher frequencies, 77 kHz, 125 kHz and 177 kHz, one can observe that the arrival-time differences jumps from −π to +π (or vice versa) in the coda part at some lag times, which is typical for cycle skipping. For the wave with a frequency of 177 kHz, cycle skipping is observed when the signal at loading step 3 is the current signal, whereas this only occurs (first) for the fourth loading step while employing the stretching technique. However, for the wave with a frequency of 77 kHz,

cycle skipping is observed for current signals at the same load step (load step 4) as the stretching technique. According to Fig. 7, the occurrence of cycle skipping in the WCS technique depends on the magnitude of the arrival-time difference and the wave frequency.

Based on the results presented in this section, it is evident that the triggers of cycle skipping in the stretching technique and the WCS technique differ. When employing the stretching technique, cycle skipping becomes apparent in time windows with low SNR. Conversely, using the WCS technique, the occurrence of cycle skipping strongly depends on the wave frequency and the magnitude of the arrival-time difference because of operating in the wavelet domain. This contrasting trigger mechanism for cycle skipping complicates the determination of which technique provides better stability. It should be noticed that the above conclusion is drawn based solely on this experiment and one should be careful generalizing these to other materials and/or significantly higher stress levels.

4.4. Comparison between the stretching technique and the WCS technique: retrieved velocity changes

Before analysing the relative *dv/v* (recall that we now estimate arrival-time changes between two consecutive loading steps; hence `the relative'), the *CC* values should be checked to ensure the reliability of the retrieved *dv/v*. The *CC* from the stretching technique is calculated for a specific time window, whereas the *CC* from the WCS technique is associated with a specific lag time and frequency. In order to compare the *CC* and *dv/v* obtained using the WCS technique to the *CC* and *dv/v* obtained using the stretching technique as a function of time, we use the same time windows adopted in the stretching technique to obtain the mean WCS technique-based relative *dv/v* and *CC* in these time windows. Along the frequency scale, the mean WCS technique-based relative *dv/v* and *CC* are calculated in two frequency bands: 50–80 kHz (low-frequency regime) and 120–180 kHz (high-frequency regime). The *CC* retrieved using the stretching technique and the WCS technique are shown in Fig. 8. The *CC* values are generally higher than 0.8 for both techniques, suggesting that the relative *dv/v* obtained from both techniques are reliable. The relatively low *CC* values in the coda of high-frequency regime shown in Fig. 8(c) are mainly attributed to the attenuation imposed low SNRs of the high-frequency waves.
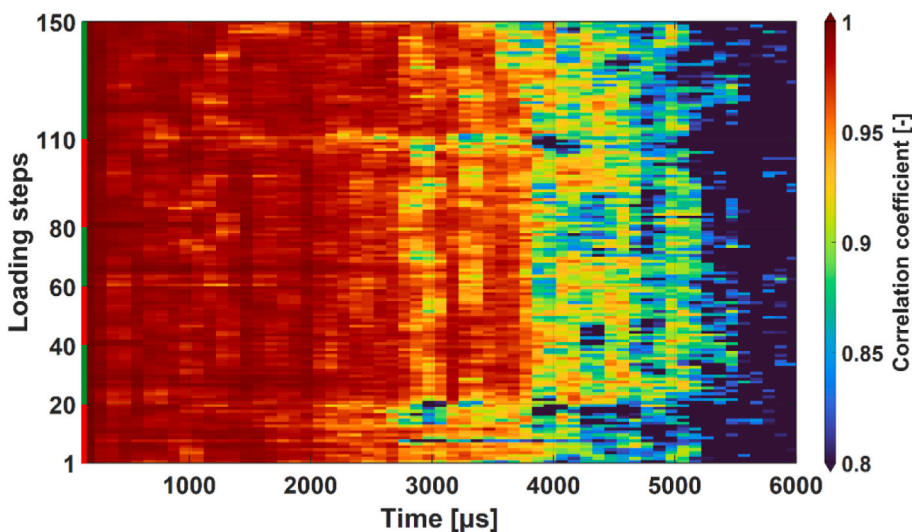
To compare the relative *dv/v* retrieved using the stretching technique and the WCS technique, the whole signal is further split into a series of
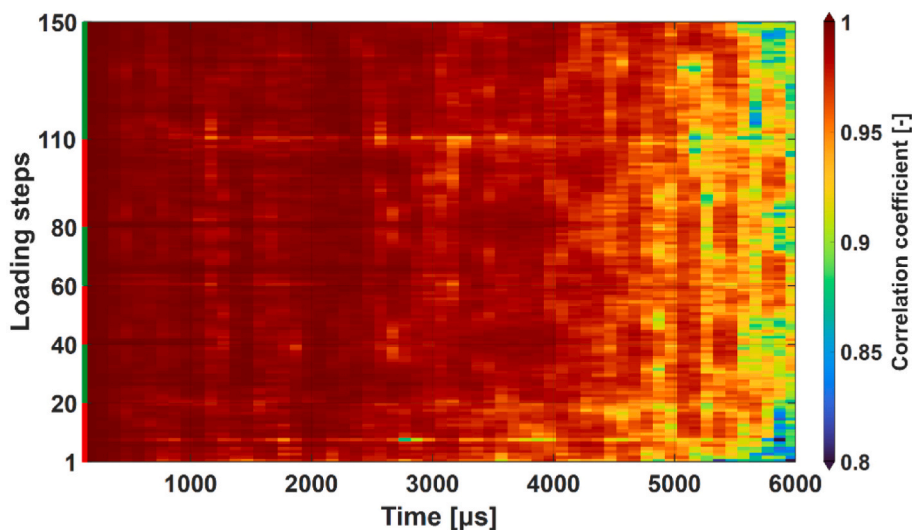
(a) *CC* obtained using the stretching technique.
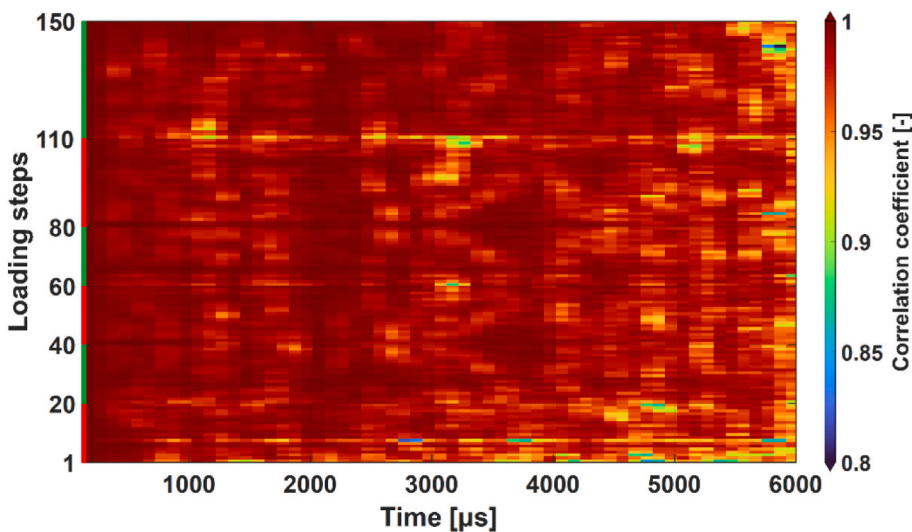
(b) *CC* within the frequency band of 50-80 kHz obtained using the WCS technique.

(c) *CC* within the frequency band of 120-180 kHz obtained using the WCS technique.

Fig. 8. *CC* at lag time and loading steps obtained using the stretching technique and the WCS technique (indicated in red on the vertical axis are the loading stages, and indicated in green the unloading stages; note that the *CC* from the WCS technique represents an average over the discrete frequencies within the frequency band). (For interpretation of the references to colour in this figure legend, the reader is referred to the web version of this article.)
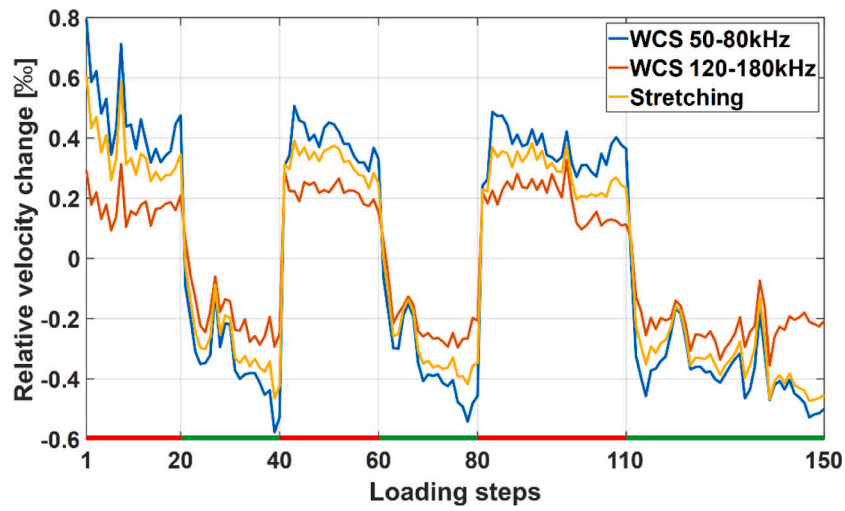
(a) Relative *dv/v* retrieved from the signal in the first time segment (first arrival-1 ms).
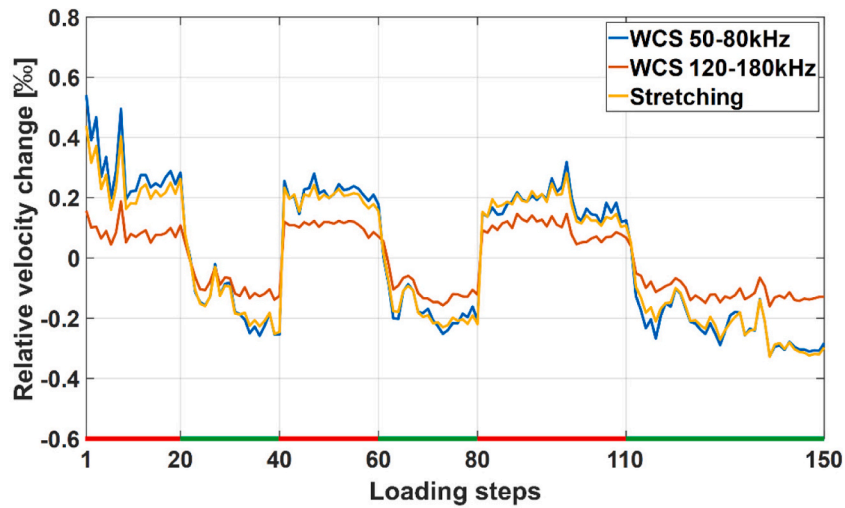
(b) Relative *dv/v* retrieved from the signal in the second time segment (1 ms-2 ms).
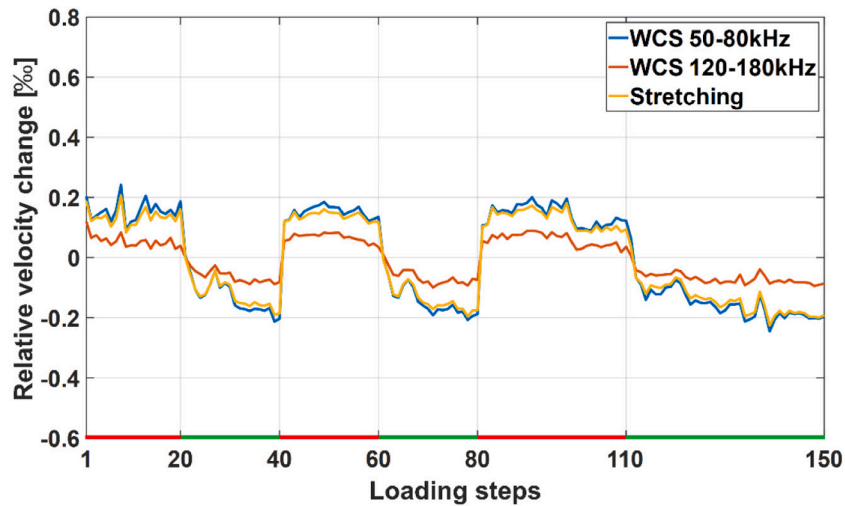
(c) Relative *dv/v* retrieved from the signal in the third time segment (2 ms-3 ms).

Fig. 9. Relative *dv/v* retrieved from the signal in different time segments as a function of loading steps (indicated in red on the horizontal axis are the loading stages, and indicated in green the unloading stages; note that the relative *dv/v* from the WCS technique represents an average over the discrete frequencies within the frequency band). (For interpretation of the references to colour in this figure legend, the reader is referred to the web version of this article.)

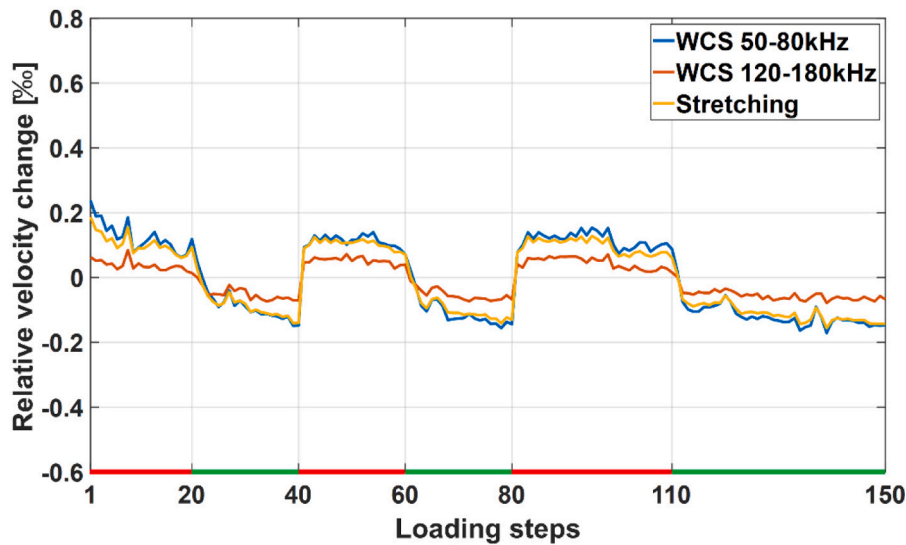(d) Relative *dv/v* retrieved from the signal in the fourth time segment (3 ms-4 ms).

Fig. 9. (*continued*).

non-overlapping time segments with a length of around 1 ms (the first time segment is from the first arrival to 1 ms). For the stretching technique and the low-frequency regime WCS, the mean relative *dv/v* of time windows with *CC* higher than 0.9 is calculated in each time segment. For the high-frequency regime WCS, the relative *dv/v* is calculated in each time segment by averaging the relative *dv/v* of time windows with *CC* higher than 0.8. The reason for using 0.8 as the *CC* threshold is that the *CC* is relatively low in the coda of the high-frequency regime.

The relative *dv/v* retrieved by the stretching technique and the WCS technique in the first four time segments are plotted in Fig. 9. The relative *dv/v* is frequency dependent, manifested by the higher relative *dv/v* retrieved from waves in the low-frequency regime (compared to the high-frequency regime). Additionally, the stretching technique-based relative *dv/v*, operating in broadband, gives intermediate values in the first time segment and is nearly equal to the *dv/v* retrieved from the low-frequency regime in the later time segments. The latter is explained by the fact that little high-frequency signal remains at greater lag time.

The vertical axis in Fig. 9 represents the relative *dv/v*, where the signal associated with the previous loading step is used as the reference. By summing these relative *dv/v* values, we obtain the accumulated *dv/v*, reflecting changes relative to the initial stress at load step 0. It is important to note that this operation is only applicable when the total velocity change is small. If there is a significant total velocity change, we recommend using a similar approach as described in Hu et al. [36]. Fig. 10 displays the trajectories of the accumulated *dv/v* retrieved using the stretching technique and the WCS technique. The accumulated *dv/v* retrieved from the stretching technique, the low-frequency regime WCS, and the high-frequency regime WCS all demonstrate a linear relationship with increasing compressive stress. However, the slopes of the accumulated *dv/v* versus compressive stress differ between different time segments.

*4.5. Comparison between the stretching technique and WCS technique: acoustoelastic effect*

To quantify the difference between the stretching and WCS techniques in terms of (approximate) linear relationship between *dv/v* and stress, the acoustoelastic parameter can be derived for each time segment. Since the P-waves and S-waves mix in the coda, the *dv/v* measured at a specific lag time of the waveform represents a weighted average of *dv/v* associated with these two wave types, with the weights

given by the amount of P- and S-wave energy present in a specific time window (which, of course, are unknown to us). Consequently, the acoustoelastic parameter obtained using Eq. (11) is also a weighted average of the acoustoelastic parameters associated with these two wave types, denoted as $\overline{A}$. The $\overline{A}$ value can be obtained by linearly fitting the *dv/v*-stress relationship. The similarity between the experimental results and the fitted results is evaluated using the coefficient of determination, R^2. Table 3 presents the $\overline{A}$ obtained through the stretching technique and the WCS technique. The $\overline{A}$ obtained using both techniques demonstrate a gradual decrease as lapse time increases. Additionally, the $\overline{A}$ retrieved from waves in the high-frequency regime is consistently lower than that obtained from waves in the low-frequency regime. In the first time segment, the stretching technique-based results yield intermediate values between low-frequency regime WCS and high-frequency regime WCS, while in the later time segments, particularly the last two, they closely resemble the WCS technique-based results in the low-frequency regime.

At this stage, it is difficult to determine whether the velocity changes retrieved using the WCS technique and the stretching technique are consistent. However, the intermediate values provided by the stretching technique suggest that the results obtained using this technique could be a combination of those retrieved using the low-frequency regime WCS and high-frequency regime WCS. In the next section, we aim to construct the velocity change retrieved using the stretching technique by combining the velocity changes derived using the WCS technique in the low-frequency and high-frequency regimes.

4.6. Comparison between the stretching technique and WCS technique: consistency in estimating velocity change

As mentioned earlier, the stretching technique determines the stretching factor, $\varepsilon_{\max}$, that maximizes the *CC*. This value can be interpreted as the mean relative velocity change, *dv/v*, of the medium. Eq. (4) reveals that both the amplitude spectrum and phase spectrum influence $|CC(t_c, T, \varepsilon)|$ and $\varepsilon_{\max}$. In contrast, the WCS technique only utilizes the phase spectrum for *dv/v* retrieval. Therefore, it is feasible to estimate the stretching technique-based result using the WCS technique-based result by incorporating the amplitude information. Eq. (3) and (4) demonstrate that the relative *dv/v* retrieved from the stretching technique is weighted by the wave energy. Consequently, it is possible to construct this relative *dv/v* by using the relative *dv/v* retrieved from the low-frequency regime
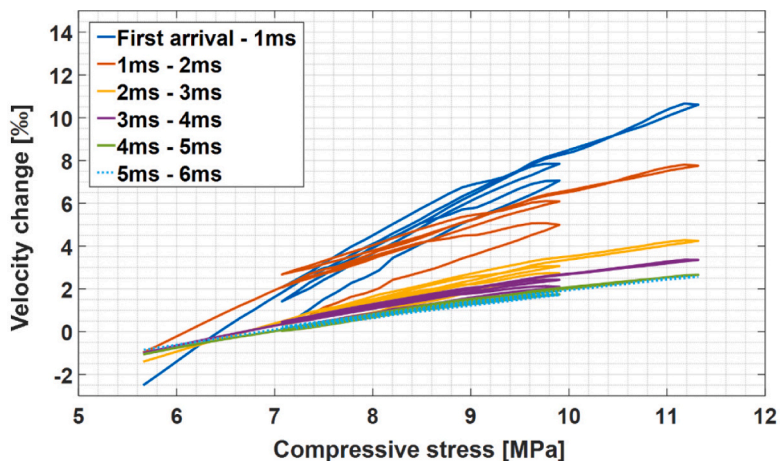
(a) Accumulated *dv/v* obtained using the stretching technique.
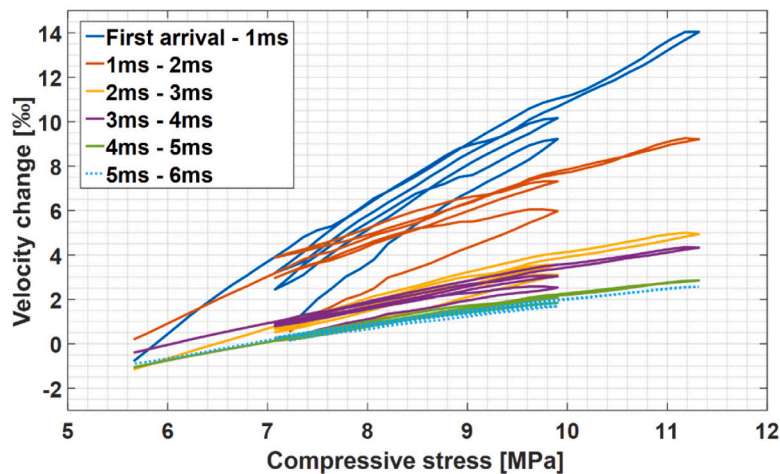
(b) Accumulated *dv/v* within the frequency band of 50-80 kHz obtained using the WCS technique.
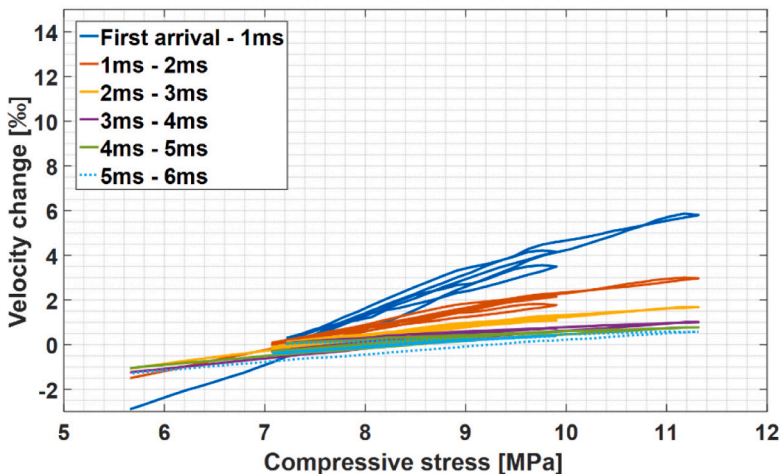
(c) Accumulated *dv/v* within the frequency band of 120-180 kHz obtained using the WCS technique.

Fig. 10. Relationship between accumulated *dv/v* vs. compressive stress in different time segments.

Table 3

$\overline{A}$ obtained through the stretching technique and the WCS technique.

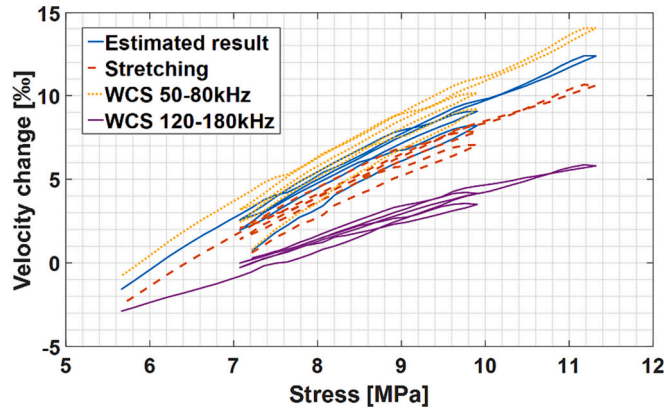| Time segment	Stretching technique		WCS technique			
			50-80 kHz		120-180 kHz	
	$\overline{A}$ [(GPa)$^{-1}$]	R^2	$\overline{A}$ [(GPa)$^{-1}$]	R^2	$\overline{A}$ [(GPa)$^{-1}$]	R^2
First arrival – 1 ms	−2.258	0.97	−2.613	0.94	−1.575	0.97
1 ms – 2 ms	−1.479	0.89	−1.554	0.85	−0.783	0.97
2 ms – 3 ms	−0.993	0.96	−1.091	0.95	−0.480	0.97
3 ms – 4 ms	−0.759	0.97	−0.846	0.94	−0.381	0.89
4 ms – 5 ms	−0.651	0.99	−0.685	0.98	−0.307	0.89
5 ms – 6 ms	−0.597	0.99	−0.598	0.98	−0.298	0.80

Fig. 11. Comparison between the estimated accumulated velocity change and those retrieved utilizing the stretching and WCS techniques in the first time segment.

WCS and high-frequency regime WCS. The estimated dv/v can be calculated using the following equation:

$$\left(\frac{\mathrm{d}v}{v}\right)_{\text{estimated}} = \frac{E_{\text{low−frequency}}}{E_{\text{low−frequency}} + E_{\text{high−frequency}}}\left(\frac{\mathrm{d}v}{v}\right)_{\text{low−frequency}} + \frac{E_{\text{high−frequency}}}{E_{\text{low−frequency}} + E_{\text{high−frequency}}}\left(\frac{\mathrm{d}v}{v}\right)_{\text{high−frequency}}, \tag{12}$$

where $(dv/v)_{\text{estimated}}$, $(dv/v)_{\text{low-frequency}}$ and $(dv/v)_{\text{high-frequency}}$ represent the estimated relative dv/v, the relative dv/v retrieved from the low-frequency regime WCS, and the relative dv/v retrieved from the high-frequency regime WCS, respectively. The $E_{\text{low-frequency}}$ and $E_{\text{high-frequency}}$ denote the wave energies (mean squared value of amplitude) of frequency bands in the low-frequency and high-frequency regimes. These energies can be directly obtained from the wavelet time-frequency spectrum. Considering that the stress condition can slightly alter the energies in frequency components of the signal, as depicted in Fig. 4, the energy of the current signal is always utilized as the weighting factor. As the intermediate value demonstrated by the stretching technique is more apparent in the first-time segment, this segment is employed to evaluate the estimated relative dv/v. However, the conclusion remains applicable to other time segments as well.

Fig. 11 presents a comparison between the estimated accumulated velocity change and those retrieved from the stretching and WCS techniques in the first time segment. The $\overline{A}$ of the estimated result is −2.437 (GPa)$^{-1}$, which is in closer agreement with the result obtained using the stretching technique. The discrepancy between the estimated and the stretching-based results can be attributed to the limited frequency

components utilized in Eq. (12), only 50-80 kHz and 120-180 kHz. Considering the challenge of including all frequency components due to the potential contamination of arrival-time changes in frequency bands with low energy [48,49], it is not feasible to incorporate every frequency in the analysis. Nevertheless, the close proximity between the estimated result and the result retrieved from the stretching technique indicates that the stretching technique-based velocity change is able to be constructed using the velocity changes retrieved from the WCS technique. Furthermore, based on Fig. 11, one can conclude that the velocity changes retrieved from the WCS technique and the stretching technique are consistent.

5. Discussion

Here, we discuss the stretching technique and the WCS technique in terms of cycle skipping, computational efficiency, future application, and some recommendations for future work.

In Section 4.3, we discussed that the causes of cycle skipping in the stretching technique and the WCS technique are somewhat different. Cycle skipping observed while employing the stretching technique is predominantly attributed to the low SNR in the coda, while the results of the WCS technique depend explicitly on the magnitude of velocity change and the selected frequency component. In a previous study [48], the authors mentioned that cycle skipping in the WCS technique could be mitigated through the process of phase unwrapping. However, they also noted that this approach may not be effective in the coda when the waveform similarity is lost. In another research paper [47], the authors identified three reasons for the occurrence of cycle skipping in the stretching technique: (i) low SNR, (ii) short time windows, and (iii) significant divergence between the two signals. Based on the experiment conducted in this study and the insights from [48], we can attribute the occurrence of cycle skipping in the WCS technique to three factors as well: (i) low SNR, (ii) signal dominated by frequencies that have a shorter period compared to the arrival-time shift, and (iii) significant divergence between the two signals. Reason (i) can also help explain why the WCS technique performs poorly in frequency bands with low energy: the SNR of the signal in these frequency bands is relatively low,

making it more susceptible to the cycle skipping and leading to less accurate retrieval of the velocity change.

In a study [49], the authors compared the performances of stretching technique and the WCS technique by applying them to the same signal within a single time window. They concluded that the stretching technique is computationally faster compared to the WCS technique when operating in a single time window. However, in our research, we observe that the retrieved velocity change exhibits lag time dependence, as reflected in different slopes of velocity change versus stress in different

Table 4

Comparison between the stretching technique and the WCS technique in the application to concrete.

CWI technique	Stretching	WCS
Operated domain	Time	Wavelet
Time-frequency resolution	Low	High
Stability against cycle skipping	Medium	Medium
Accuracy	High	High*
Computational efficiency	Low	High
Capability to handle noisy signals	Low	High

Note: * only valid when the signal energy at frequencies of interest is high.

time segments. Therefore, we suggest using multiple overlapping time windows for the stretching operation to capture this lag time-dependent behaviour. However, a drawback of using multiple time windows is the significant increase in computational cost. On the other hand, the WCS technique operates in the wavelet domain and directly retrieves the velocity change at each lapse time from the phase spectrum. Considering the time-dependent nature of retrieved velocity change, the WCS technique offers higher computational efficiency compared to the stretching technique in the application to concrete.

In Wang et al. [62], a possible solution for noise reduction in the application of CWI is proposed. This approach involves filtering the signal before applying the stretching technique. While this operation effectively reduces the impact of noise, it introduces additional computational costs due to the signal filtering process, which in turn slows down the computational speed. On the other hand, wavelet decomposition, a tool for time-frequency analysis, implicitly acts as a filter by allowing selective focus on a specific frequency band where the signal energy is sufficiently high. This allows the WCS technique to effectively reduce the influence of noise without the need for additional signal filtering.

Table 4 presents a comparative analysis of the stretching technique and the WCS technique when applied to concrete. This assessment is derived from the research findings detailed in this paper and takes into account factors such as computational efficiency and the ability to handle noisy signals, as discussed in this section.

Through our utilization of the WCS technique, we observe that waves in the low-frequency regime display a more pronounced acoustoelastic effect compared to those in the high-frequency regime. This observation can potentially be explained by the characteristics of concrete as a material with significant heterogeneity. Low-frequency waves are less sensitive to small-scale (sub-wavelength) heterogeneity and hence undergoes less scattering, as such having a higher likelihood of maintaining the original propagation direction, which, in our experiment, is parallel to the applied stress and thus most affected by the acoustoelastic effect. In summary, the different acoustoelastic effects experienced by waves at different frequencies is a result of the combination of concrete heterogeneity and acoustoelasticity. Further validation of this statement will be pursued in our future work.

Another interesting topic for future research is the further investigation of the acoustoelastic effect in concrete. Although this paper demonstrates the presence of the acoustoelastic effect even in the later coda, it is noteworthy that the slope of the velocity change versus stress in this part differs to that in the direct wave part. Understanding this variation of the acoustoelastic effect is crucial for the application of CWI in stress monitoring of concrete structures. However, due to the complexity of wave polarization, propagation, and the involvement of multiple scattering in the coda, the nature of the acoustoelastic effect in the coda remains an open question [9]. In our future work, we will delve deeper into this topic and try to shed light on this phenomenon.

6. Conclusion

This paper compares the performance of two CWI techniques, the

WCS technique and the stretching technique, in measuring the stress-induced velocity change in a concrete cylindrical sample. The embeddable piezoelectric sensor, called smart aggregates, is used to generate and detect the elastic wave. The comparison of these techniques is conducted from two perspectives: stability against cycle skipping and consistency in retrieving velocity change.

When utilizing the stretching technique, cycle skipping is observed in time windows with low SNR. On the other hand, the occurrence of cycle skipping in the WCS technique is highly dependent on the wave frequency and magnitude of velocity change. This discrepancy in the mechanisms triggering cycle skipping makes it challenging to determine which technique offers better stability. However, when examining the performance of these techniques specifically for wave frequencies ranging from 50 kHz to 80 kHz in this particular case, their stability is found to be comparable.

The velocity change retrieved using the stretching technique yields an intermediate value between those obtained from the low-frequency regime WCS and high-frequency regime WCS in the initial time segments. Furthermore, it closely aligns with the velocity change retrieved in the low-frequency regime in the later time segments. The intermediate value arises because the stretching technique captures the arrival-time change experienced by all frequencies. Expressing the stretching technique in the frequency domain reveals that both the amplitude and phase spectra are utilized. In contrast, the WCS technique only requires the phase spectra. Consequently, the velocity change retrieved from the stretching technique represents a weighted average of the arrival-time changes at each frequency, with the wave energy serving as the weight. This conclusion also elucidates the high similarity observed between the results obtained by the stretching technique and the low-frequency regime WCS technique in the later time segments. One can construct the velocity change retrieved from the stretching technique by weighting the velocity changes from the WCS technique using wave energies. The constructed outcome suggests that the velocity changes retrieved using these two CWI techniques are consistent.

When it comes to the future application of CWI techniques in concrete stress monitoring, it is recommended to determine the suitable time window length for the stretching technique by considering both the wave frequency and the expected magnitude of velocity change. Similarly, for the WCS technique, it is advisable to determine the operational frequency band by considering the expected magnitude of velocity change and the energy present within the frequency band.

Declaration of Competing Interest

The authors declare that they have no known competing financial interests or personal relationships that could have appeared to influence the work reported in this paper.

Data availability

Data will be made available on request.

Appendix A. Parseval's theorem

Parseval's theorem is used to express the correlation coefficients in the frequency domain. We show the continuous case below, but the proof is similar for the discrete case. For two signals $x(t)$ and $y(t)$ and their Fourier transforms $X(f)$ and $Y(f)$, we have the following relation

$$\int_{-\infty}^{+\infty} x(t)y(t)dt$$

$$= \int_{-\infty}^{+\infty} x(t)\left[\int_{-\infty}^{+\infty} Y(f)e^{j2\pi ft}df\right]dt$$

$$= \int_{-\infty}^{+\infty} Y(f)\left[\int_{-\infty}^{+\infty} x(t)e^{j2\pi ft}dt\right]df \qquad\qquad (A1)$$

$$= \int_{-\infty}^{+\infty} Y(f)X(-f)df$$

$$= \int_{-\infty}^{+\infty} Y(f)X^*(f)df,$$

where the asterisk denotes complex conjugation.

References

[1] S.K.U. Rehman, Z. Ibrahim, S.A. Memon, M. Jameel, Nondestructive test methods for concrete bridges: a review, Constr. Build. Mater. 107 (2016) 58–86, https://doi.org/10.1016/j.conbuildmat.2015.12.011.

[2] P. Rizzo, A. Enshaeian, Bridge health monitoring in the United States: a review, Struct. Monit. Mainten. 8 (1) (2021) 1–50, https://doi.org/10.12989/smm.2021.8.1.001.

[3] H. Jiang, J. Zhang, R. Jiang, Stress evaluation for rocks and structural concrete members through ultrasonic wave analysis: review, J. Mater. Civ. Eng. 29 (10) (2017) 04017172, https://doi.org/10.1061/(ASCE)MT.1943-5533.0001935.

[4] S. Taheri, A review on five key sensors for monitoring of concrete structures, Constr. Build. Mater. 204 (2019) 492–509, https://doi.org/10.1016/j.conbuildmat.2019.01.172.

[5] S. Biswal, A. Ramaswamy, Measurement of existing prestressing force in concrete structures through an embedded vibrating beam strain gauge, Measurement 83 (2016) 10–19, https://doi.org/10.1016/j.measurement.2016.01.031.

[6] M. Majumder, T.K. Gangopadhyay, A.K. Chakraborty, K. Dasgupta, D. K. Bhattacharya, Fibre Bragg gratings in structural health monitoring - present status and applications, Sensors Actuators A Phys. 147 (1) (2008) 150–164, https://doi.org/10.1016/j.sna.2008.04.008.

[7] A. Barrias, J.R. Casas, S. Villalba, A review of distributed optical fiber sensors for civil engineering applications, Sensors 16 (5) (2016) 748, https://doi.org/10.3390/s16050748.

[8] M.A. Sutton, J.J. Orteu, H.W. Schreier, Image Correlation for Shape, Motion and Deformation Measurements: Basic Concepts, Theory and Applications, Springer, New York, 2009. ISBN: 978-0-387-78746-6.

[9] T. Planes, E. Larose, A review of ultrasonic coda wave interferometry in concrete, Cem. Concr. Res. 53 (2013) 248–255, https://doi.org/10.1016/j.cemconres.2013.07.009.

[10] S. Grabke, F. Clauss, K.U. Bletzinger, M.A. Ahrens, P. Mark, R. Wuchner, Damage detection at a reinforced concrete specimen with coda wave interferometry, Materials 14 (17) (2021) 5013, https://doi.org/10.3390/ma14175013.

[11] C. Dumoulin, A. Deraemaeker, All-season monitoring of concrete repair in an urban tunnel in Brussels using embedded ultrasonic transducers with emphasis on robustness to environmental variations, J. Civ. Struct. Heal. Monit. 11 (4) (2021) 879–895, https://doi.org/10.1007/s13349-021-00486-9.

[12] Y. Zhang, E. Larose, L. Moreau, G. d'Ozouville, Three-dimensional in-situ imaging of cracks in concrete using diffuse ultrasound, Struct. Health Monit. 17 (2) (2018) 279–284, https://doi.org/10.1177/1475921717690938.

[13] R. Snieder, A. Gret, H. Douma, J. Scales, Coda wave interferometry for estimating nonlinear behavior in seismic velocity, Science 295 (5563) (2002) 2253–2255, https://doi.org/10.1126/science.1070015.

[14] R. Snieder, The theory of coda wave interferometry, Pure Appl. Geophys. 163 (2–3) (2006) 455–473, https://doi.org/10.1007/s00024-005-0026-6.

[15] K. Aki, Analysis of the seismic coda of local earthquakes as scattered waves, J. Geophys. Res. 74 (2) (1969) 615–631, https://doi.org/10.1029/JB074i002p00615.

[16] K. Aki, B. Chouet, Origin of coda waves: source, attenuation, and scattering effects, J. Geophys. Res. 80 (23) (1975) 3322–3342, https://doi.org/10.1029/JB080i023p03322.

[17] X. Wang, J. Chakraborty, A. Bassil, E. Niederleithinger, Detection of multiple cracks in four-point bending tests using the coda wave interferometry method, Sensors 20 (7) (2020) 1986, https://doi.org/10.3390/s20071986.

[18] D.S. Hughes, J. Kelly, Second-order elastic deformation of solids, Phys. Rev. 92 (5) (1953) 1145.

[19] R. Toupin, B. Bernstein, Sound waves in deformed perfectly elastic materials. Acoustoelastic effect, J. Acoustic. Soc. Am. 33 (2) (1961) 216–225, https://doi.org/10.1121/1.1908623.

[20] R. Thurston, K. Brugger, Third-order elastic constants and the velocity of small amplitude elastic waves in homogeneously stressed media, Phys. Rev. 133 (6A) (1964) A1604–A1610, https://doi.org/10.1103/PhysRev.133.A1604.

[21] S.C. Stahler, C. Sens-Schonfelder, E. Niederleithinger, Monitoring stress changes in a concrete bridge with coda wave interferometry, J. Acoust. Soc. Am. 129 (4) (2011) 1945–1952, https://doi.org/10.1121/1.3553226.

[22] E. Larose, S. Hall, Monitoring stress related velocity variation in concrete with a 2×10^{-5} relative resolution using diffuse ultrasound, J. Acoust. Soc. Am. 125 (4) (2009) 1853–1856, https://doi.org/10.1121/1.3079771.

[23] C. Payan, V. Garnier, J. Moysan, P.A. Johnson, Determination of third order elastic constants in a complex solid applying coda wave interferometry, Appl. Phys. Lett. 94 (1) (2009), 011904, https://doi.org/10.1063/1.3064129.

[24] C. Payan, V. Garnier, J. Moysan, Potential of nonlinear ultrasonic indicators for nondestructive testing of concrete, Adv. Civ. Eng. 2010 (2010), 238472, https://doi.org/10.1155/2010/238472.

[25] I. Lillamand, J.F. Chaix, M.A. Ploix, V. Garnier, Acoustoelastic effect in concrete material under uni-axial compressive loading, NDT & E Int. 43 (8) (2010) 655–660, https://doi.org/10.1016/j.ndteint.2010.07.001.

[26] C. Payan, V. Garnier, J. Moysan, Determination of nonlinear elastic constants and stress monitoring in concrete by coda waves analysis, Eur. J. Environ. Civ. Eng. 15 (4) (2011) 519–531, https://doi.org/10.3166/EJECE.15.519-531.

[27] D.P. Schurr, J.Y. Kim, K.G. Sabra, L.J. Jacobs, Damage detection in concrete using coda wave interferometry, NDT & E Int. 44 (8) (2011) 728–735, https://doi.org/10.1016/j.ndteint.2011.07.009.

[28] Y. Zhang, O. Abraham, F. Grondin, A. Loukili, V. Tournat, A. Le Duff, B. Lascoup, O. Durand, Study of stress-induced velocity variation in concrete under direct tensile force and monitoring of the damage level by using thermally-compensated Coda Wave Interferometry, Ultrasonics 52 (8) (2012) 1038–1045, https://doi.org/10.1016/j.ultras.2012.08.011.

[29] Y. Zhang, O. Abraham, V. Tournat, A. Le Duff, B. Lascoup, A. Loukili, F. Grondin, O. Durand, Validation of a thermal bias control technique for Coda Wave Interferometry (CWI), Ultrasonics 53 (3) (2013) 658–664, https://doi.org/10.1016/j.ultras.2012.08.003.

[30] Y. Zhang, T. Planes, E. Larose, A. Obermann, C. Rospars, G. Moreau, Diffuse ultrasound monitoring of stress and damage development on a 15-ton concrete beam, J. Acoust. Soc. Am. 139 (4) (2016) 1691–1701, https://doi.org/10.1121/1.4945097.

[31] J. Zhang, B. Han, H. Xie, L. Zhu, G. Zheng, W. Wang, Correlation between coda wave and stresses in uni-axial compression concrete, Appl. Sci. 8 (9) (2018) 1609, https://doi.org/10.3390/app8091609.

[32] F. Clauß, N. Epple, M.A. Ahrens, E. Niederleithinger, P. Mark, Comparison of experimentally determined two-dimensional strain fields and mapped ultrasonic data processed by coda wave interferometry, Sensors 20 (14) (2020) 4023, https://doi.org/10.3390/s20144023.

[33] H. Jiang, H. Zhan, Z. Ma, R. Jiang, Comparative study of three-dimensional stress and crack imaging in concrete by application of inverse algorithms to coda wave measurements, Sensors 20 (17) (2020) 4899, https://doi.org/10.3390/s20174899.

[34] H. Zhan, H. Jiang, J. Zhang, R. Jiang, Condition evaluation of an existing T-beam bridge based on neutral axis variation monitored with ultrasonic coda waves in a network of sensors, Sensors 20 (14) (2020) 3895, https://doi.org/10.3390/s20143895.

[35] H. Zhan, H. Jiang, C. Zhuang, J. Zhang, R. Jiang, Estimation of stresses in concrete by using coda wave interferometry to establish an acoustoelastic modulus database, Sensors 20 (14) (2020) 4031, https://doi.org/10.3390/s20144031.

[36] H. Hu, D. Li, L. Wang, R. Chen, X. Xu, An improved ultrasonic coda wave method for concrete behavior monitoring under various loading conditions, Ultrasonics 116 (2021), 106498, https://doi.org/10.1016/j.ultras.2021.106498.

[37] H. Jiang, H. Zhan, J. Zhang, R. Jiang, C. Zhuang, P. Fan, Detecting stress changes and damage in full-size concrete t-beam and slab with ultrasonic coda waves, J. Struct. Eng. 147 (9) (2021) 04021140, https://doi.org/10.1061/(ASCE)ST.1943-541X.0003090.

[38] Q. Xue, E. Larose, L. Moreau, R. Thery, O. Abraham, J.M. Henault, Ultrasonic monitoring of stress and cracks of the 1/3 scale mock-up of nuclear reactor concrete containment structure, Struct. Health Monit. 21 (4) (2021) 1474–1482, https://doi.org/10.1177/14759217211034729.

[39] B. Zhong, J. Zhu, G. Morcous, Measuring acoustoelastic coefficients for stress evaluation in concrete, Constr. Build. Mater. 309 (2021) 125127, https://doi.org/10.1016/j.conbuildmat.2021.125127.

[40] F. Diewald, N. Epple, T. Kraenkel, C. Gehlen, E. Niederleithinger, Impact of external mechanical loads on coda waves in concrete, Materials 15 (16) (2022) 5482, https://doi.org/10.3390/ma15165482.

[41] Y. He, L. Song, K. Xue, S. Liu, H. Li, W. Yang, J. Huang, Ultrasonic coda wave experiment and simulation of concrete damage process under uniaxial

compression, Buildings 12 (5) (2022) 514, https://doi.org/10.3390/buildings12050514.

[42] B. Zhong, J. Zhu, Applications of stretching technique and time window effects on ultrasonic velocity monitoring in concrete, Appl. Sci. 12 (14) (2022) 7130, https://doi.org/10.3390/app12147130.

[43] A. Grêt, R. Snieder, U. Özbay, Monitoring in situ stress changes in a mining environment with coda wave interferometry, Geophys. J. Int. 167 (2) (2006) 504–508, https://doi.org/10.1111/j.1365-246X.2006.03097.x.

[44] J. Frechet, L. Martel, L. Nikolla, G. Poupinet, Application of the Cross-Spectral Moving-Window Technique (CSMWT) to the seismic monitoring of forced fluid migration in a rock mass, Int. J. Rock Mech. Min. Sci. Geomech. Abstr. 26 (3–4) (1989) 221–233, https://doi.org/10.1016/0148-9062(89)91972-4.

[45] G. Poupinet, W. Ellsworth, J. Frechet, Monitoring velocity variations in the crust using earthquake doublets: an application to the Calaveras Fault, California, J. Geophys. Res. Solid Earth 89 (B7) (1984) 5719–5731, https://doi.org/10.1029/JB089iB07p05719.

[46] C. Sens-Schonfelder, U. Wegler, Passive image interferometry and seasonal variations of seismic velocities at Merapi Volcano, Indonesia, Geophys. Res. Lett. 33 (21) (2006) L21302, https://doi.org/10.1029/2006GL027797.

[47] T.D. Mikesell, A.E. Malcolm, D. Yang, M.M. Haney, A comparison of methods to estimate seismic phase delays: numerical examples for coda wave interferometry, Geophys. J. Int. 202 (1) (2015) 347–360, https://doi.org/10.1093/gji/ggv138.

[48] S. Mao, A. Mordret, M. Campillo, H. Fang, R.D. van der Hilst, On the measurement of seismic traveltime changes in the time-frequency domain with wavelet cross-spectrum analysis, Geophys. J. Int. 221 (1) (2020) 550–568, https://doi.org/10.1093/gji/ggz495.

[49] C. Yuan, J. Bryan, M. Denolle, Numerical comparison of time-, frequency-and wavelet-domain methods for coda wave interferometry, Geophys. J. Int. 226 (2) (2021) 828–846, https://doi.org/10.1093/gji/ggab140.

[50] O.I. Lobkis, R.L. Weaver, Coda-wave interferometry in finite solids: recovery of P-to-S conversion rates in an elastodynamic billiard, Phys. Rev. Lett. 90 (25) (2003), 254302, https://doi.org/10.1103/PhysRevLett.90.254302.

[51] Z. Zhan, V.C. Tsai, R.W. Clayton, Spurious velocity changes caused by temporal variations in ambient noise frequency content, Geophys. J. Int. 194 (3) (2013) 1574–1581, https://doi.org/10.1093/gji/ggt170.

[52] P.C. Liu, Wavelet spectrum analysis and ocean wind waves, Wavelet Anal. Appl. 4 (1994) 151–166, https://doi.org/10.1016/B978-0-08-052087-2.50012-8.

[53] C. Hadziioannou, E. Larose, O. Coutant, P. Roux, M. Campillo, Stability of monitoring weak changes in multiply scattering media with ambient noise correlation: laboratory experiments, J. Acoust. Soc. Am. 125 (6) (2009) 3688–3695, https://doi.org/10.1121/1.3125345.

[54] J. Morlet, G. Arens, E. Fourgeau, D. Giard, Wave propagation and sampling theory; Part II: sampling theory and complex waves, Geophysics 47 (2) (1982) 222–236, https://doi.org/10.1190/1.1441329.

[55] J. Morlet, G. Arens, E. Fourgeau, D. Glard, Wave propagation and sampling theory; Part I: Complex signal and scattering in multilayered media, Geophysics 47 (2) (1982) 203–221, https://doi.org/10.1190/1.1441328.

[56] M. Farge, Wavelet transforms and their applications to turbulence, Annu. Rev. Fluid Mech. 24 (1) (1992) 395–458, https://doi.org/10.1146/annurev.fl.24.010192.002143.

[57] C. Torrence, G.P. Compo, A practical guide to wavelet analysis, Bull. Am. Meteorol. Soc. 79 (1) (1998) 61–78, https://doi.org/10.1175/1520-0477(1998)079<0061:APGTWA>2.0.CO;2.

[58] F. Glangeaud, Signal processing for magnetic pulsations, J. Atmos. Terres. Phys. 43 (9) (1981) 981–998, https://doi.org/10.1016/0021-9169(81)90088-X.

[59] Y.H. Pao, U. Gamer, Acoustoelastic waves in orthotropic media, J. Acoust. Soc. Am. 77 (3) (1985) 806–812, https://doi.org/10.1121/1.392384.

[60] C.L. Nogueira, K.L. Rens, Acoustoelastic response of concrete under uniaxial compression, ACI Mater. J. 116 (3) (2019) 21–33, https://doi.org/10.14359/51714462.

[61] G. Song, H. Gu, Y.L. Mo, T.T.C. Hsu, H. Dhonde, Concrete structural health monitoring using embedded piezoceramic transducers, Smart Mater. Struct. 16 (4) (2007) 959–968, https://doi.org/10.1088/0964-1726/16/4/003.

[62] X. Wang, J. Chakraborty, E. Niederleithinger, Noise reduction for improvement of ultrasonic monitoring using coda wave interferometry on a real bridge, J. Nondestruct. Eval. 40 (1) (2021) 14, https://doi.org/10.1007/s10921-020-00743-9.

[63] X. Wang, E. Niederleithinger, I. Hindersmann, The installation of embedded ultrasonic transducers inside a bridge to monitor temperature and load influence using coda wave interferometry technique, Struct. Health Monit. 21 (3) (2021) 913–927, https://doi.org/10.1177/14759217211014430.

[64] S.W. Shin, C.B. Yun, J.S. Popovics, J.H. Kim, Improved Rayleigh wave velocity measurement for nondestructive early-age concrete monitoring, Res. Nondestruct. Eval. 18 (1) (2007) 45–68, https://doi.org/10.1080/09349840601128762.

[65] V. Giurgiutiu, J. Bao, W. Zhao, Active sensor wave propagation health monitoring of beam and plate structures, in: Smart Structures and Materials 2001: Smart Structures and Integrated Systems Vol. 4327, International Society for Optics and Photonics, 2001, pp. 234–245, https://doi.org/10.1117/12.436535.

[66] Q. Kong, Innovation in Piezoceramic Based Structural Health Monitoring (Doctoral dissertation), University of Houston, 2015. URL, http://hdl.handle.net/10657/3664 (Accessed January 2022).

[67] V. Rossetto, L. Margerin, T. Planès, E. Larose, Locating a weak change using diffuse waves: theoretical approach and inversion procedure, J. Appl. Phys. 109 (3) (2011), 034903, https://doi.org/10.1063/1.3544503.

[68] C. Torrence, P.J. Webster, Interdecadal changes in the ENSO-monsoon system, J. Clim. 12 (8) (1999) 2679–2690, https://doi.org/10.1175/1520-0442(1999)012<2679:ICITEM>2.0.CO;2.